SANDIA REPORT
SAND2019-9998
Printed August, 2019

Sandia National Laboratories

Characteristics of Cryogenic Hydrogen Releases Under Unignited and Ignited Conditions

Ethan S. Hecht, Pratikash P. Panda, Bikram Roy Chowdhury, Dongmei Ye

Prepared by
Sandia National Laboratories
Albuquerque, New Mexico 87185
Livermore, California 94550

Issued by Sandia National Laboratories, operated for the United States Department of Energy by National Technology & Engineering Solutions of Sandia, LLC.

Available to DOE and DOE contractors from

U.S. Department of Energy
Office of Scientific and Technical Information
P.O. Box 62
Oak Ridge, TN 37831

Telephone: (865) 576-8401
Facsimile: (865) 576-5728
E-Mail: reports@osti.gov
Online ordering: http://www.osti.gov/scitech

Available to the public from

U.S. Department of Commerce
National Technical Information Service
5301 Shawnee Road
Alexandria, VA 22312

Telephone: (800) 553-6847
Facsimile: (703) 605-6900
E-Mail: orders@ntis.gov
Online order: https://classic.ntis.gov/help/order-methods

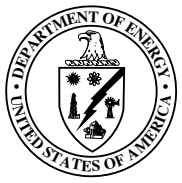

ABSTRACT

Hydrogen is increasingly being used in the public sector as a fuel for vehicles. Due to the high density of hydrogen in its liquid phase, fueling stations that receive deliveries of and store hydrogen as a liquid are more practical for high volume stations. There is a critical need for validated models to assess the risk at hydrogen fueling stations with cryogenic hydrogen on-site. In this work, a cryogenic hydrogen release experiment generated controlled releases of cryogenic hydrogen in the laboratory. We measured the maximum ignition distance, flame length and the radiative heat flux and developed correlations to calculate the ignition ditance and the radiative heat flux. We also measured the concentration and temperature fields of releases under unignited conditions and used these measurements to validate a model for these cryogenic conditions. This study provides critical information on the development of models to inform the safety codes and standards of hydrogen infrastructure.

ACKNOWLEDGMENT

The U.S. Department of Energy's (DOE) office of Energy Efficiency and Renewable Energy's (EERE) Fuel Cell Technologies Office (FCTO) supports the development of science-based codes and standards through the Safety, Codes and Standards program element. The authors gratefully acknowledge funding from FCTO to support the work described in this report. The authors would like to acknowledge the support of subprogram manager Laura Hill. The authors appreciate additional financial support through a cooperative research and development agreement with BKi and the Fire Protection Research Foundation with funding from the CaFCP Auto OEM Group, Linde and Shell. The authors also wish to thank Radoslav Bozinoski for updating COLDPLUME to a Python version.

CONTENTS

LIST OF FIGURES

LIST OF TABLES

1. INTRODUCTION

Hydrogen is increasingly being used in the public sector as a fuel for vehicles, with ambitious targets for growth. In California, the large and growing network of stations is mapped by the California Fuel Cell Partnership [1]. Aggressive construction of fueling stations is needed to support the growing number of fuel cell electric vehicles [2, 3]. Heavy-duty vehicles (trucks) have also been targeted as a prime market for hydrogen fuel cell powertrains [4]. Significant infrastructure upgrades to accommodate increased bulk transport, storage, and delivery will be required on exiting fueling stations. Urban centers, including San Francisco, Los Angeles, and San Diego (in California, with additional urban centers on the east coast such as Boston and New York) will need to have large fueling stations, able to dispense fuel to many vehicles daily. In order to have sufficient hydrogen on-site (300–1000 kg/day), and a sustainable method of hydrogen delivery, hydrogen at many stations will likely be delivered and stored as a liquid due to the high density of hydrogen in its liquid phase.

In urban areas, siting of liquid hydrogen fueling infrastructure for Fuel Cell Electric Vehicles (FCEV) are limited to space-constrained sites, which stimulated an interest in placing bulk cryogenic hydrogen storage at reduced separation distances. The safety codes developed for traditional industrial uses of flammable cryogens were established on lots that can accommodate large safety separation distances, which contrast with this new space-constrained storage requirement. Moreover, the current prescriptive liquid hydrogen separation distances are based on subjective expert opinion rather than physical models. Even though Safety for hydrogen infrastructure is of utmost importance, the current liquid hydrogen bulk storage separation distances for lot lines, building openings or air intakes, may be overly conservative as reported in 2016 edition of National Fire Protection Agency Hydrogen Technologies Code (NFPA 2) [5]. The goal of this work is to advance the scientific understanding of the thermo-physical characteristics of cryogenic hydrogen releases and flames to the point where codes and standards can be informed by the physics of these phenomena.

1.1. Current fire codes and standards for liquid hydrogen use

The fire codes that govern hydrogen use, such as NFPA 2: Hydrogen Technologies Code [5], have challenging separation distance requirements for liquid hydrogen. A typical liquid hydrogen storage tank operating pressure is 1-5 bar and the density of liquid hydrogen is approximately 70 kg/l. In order to have 1000 kg hydrogen on a site, a station would need to have a tank of approximately 15,000 l. A tank of this size requires 15 m of separation from lot lines, ignition sources, sprinklered buildings of combustible construction, and overhead utilities [5]. It also requires 23 m of separation from building openings, places of public assembly, unsprinklered buildings of combustible construction, and other combustible liquids or gases (e.g., gasoline tanks) [5]. While fire barrier walls can be used to reduce separation distances to lot lines, buildings, and other combustible liquids or gases, there are currently no mitigations for reducing the 23 m separation distance to building openings/air intakes or places of public assembly, or the 15 m separation distance from ignition sources or overhead utilities. The 23 m separation distance

can be especially challenging to meet in urban centers, where the high vehicle throughput necessitates large quantities of hydrogen storage enabled by liquid hydrogen.

1.2. Cryogenic hydrogen behavior models

As discussed in Annexes E and I of NFPA 2 [5], the separation distances for gaseous hydrogen are based on a risk-informed process, which is described by LaChance [6] and LaChance et al. [7]. This risk-informed process relies on data of leak frequency and size coupled to behavior models of hydrogen dispersion and flames, and thus helps develop the code requirements of the minimum separation distances at hydrogen facilities to acceptable levels. In order to re-evaluate the minimum separation distances for liquid hydrogen systems, scientific analyses using validated behavior models for cryogenic hydrogen are needed.

Codes and standards development that governs the storage and transport of liquid hydrogen requires a thorough understanding of release and dispersion characteristics, along with flammability and radiation heat transfer over a range of realistic scenarios and environmental conditions [8]. It is also important to consider specific activities, such as repeated fuel transfer connections being made or broken. Most hydrogen releases are highly turbulent and heavily influenced by buoyancy. Cryogenic hydrogen dispersion can be affected by many situations, such as flashing, multi-phase flows, heat transfer, pool formation, ambient conditions (e.g., temperature, humidity, wind), ground effects, and obstacles/barriers. Extreme cold temperatures can also condense or even freeze ambient air during spills, which differentiates these releases from those of liquid natural gas and can result in unique hazards that need to be understood as well [9, 10]. A review of hydrogen system safety knowledge by Kotchourko et al. [11] includes a detailed discussion of liquid hydrogen systems. Several research priorities and knowledge gaps were identified to enable accurate modeling of liquid hydrogen releases for safety analyses. Hall et al. [12] reported experimental studies to establish the severity of an ignition from a release of LH2, using spill rates consistent with a transfer hose operation. However, they only created a safety distance guide which corresponds to their hydrogen spillage rate. While several large-scale studies have looked at the pooling and vaporization of hydrogen [9–13], these experiments are sparsely instrumented with poorly controlled boundary conditions. The use of improperly validated models to establish safety envelopes could be detrimental to the emergence of hydrogen as a transportation fuel.

There are several groups who have performed modeling of cryogenic hydrogen dispersion and attempted to validate their models. These works include Schmidtchen and coworkers [14, 15], Middha and colleagues [16–18], Giannissi and coworkers [19–21], and Jin et al. [22, 23]. The validation data for these models are based on three sets of experiments: spill tests performed by the National Aeronautics and Space Administration (NASA) [24], pool spreading and vaporization experiments performed by Germany's Federal Institute for Materials Research and Testing (BAM) [25], and a set of release experiments at the U.K.'s Health and Safety Laboratory (HSL) [9, 10]. However, each of these three experimental setups had limited concentration measurements with poor spatial resolution and varying boundary (e.g. wind) conditions during the releases, making the data unsuitable for quantitative model validation.

Xiao et al. [26] measured hydrogen centerline concentration decay from a 298 and 80 K reservoir flowing through 1–2 mm diameter nozzles at an FZK facility. The authors were able to show good agreement with an integral model. Winters and Houf [27, 28] developed a model for simulating liquid hydrogen releases. While this model compared favorably to the Xiao et al. data [26], it has not been validated for hydrogen releases at temperatures below 80 K, where the components of air begin to condense. Further, only hydrogen centerline concentration predictions were compared to experiments, and the rate of hydrogen dispersion radially has not been studied.

In a controlled laboratory conditions, Freidrich et al. [29] measured hydrogen centerline concentration decay at some discrete points for 34–65 K hydrogen at up to 30 bar at the Karlsruhe Institute of Technology. They found that the concentration decayed slower for cold release (34-65 K) than for the warmer releases (290 and 80 K). Other than these two experiments, there is a dearth of data suitable for hydrogen concentration modeling validation under well controlled boundary conditions.

1.3. Method overview

The goal of this work is to advance the scientific understanding of the thermo-physical characteristics of cryogenic hydrogen releases and flames to the point where codes and standards can be informed by the physics of these phenomena. As discussed by LaChance et al. [7], the radiant heat flux from a jet flame is a critical parameter that governs the deterministic separation distance (or the hazard distance) to prevent harm during an accident scenario. A maximum ignition distance (X_{ign}) is defined as the maximum distance from the nozzle exit at which a laser spark causes upstream flame propagation, leading to a sustained jet flame. An understanding of the ignition distance can inform other separation distances, such as the distance hydrogen infrastructure should be kept from ignition sources (e.g., power lines).

We began this work by studying at the ignition and flame characteristics of cryogenic hydrogen releases, then we focused on the unignited concentration fields of cryogenic hydrogen releases. A cryogenic hydrogen release facility was designed, constructed and used in this work to simulate leak scenarios from a liquid hydrogen storage system. The experimental facility was designed for a controlled, steady-state release at fixed pressure and temperature. Cold (as low as 37 K) hydrogen releases formed under-expanded jets, which were subsequently ignited with a laser generated spark. The ignition distance, X_{ign}, was measured. The radiative power from the sustained turbulent diffusion jet flames was measured as well using radiometers. We have developed correlations using the flow variables to calculate the X_{ign} and radiant heat flux from ignited flames of cryogenic, under-expanded hydrogen jets.

We have also investigated the dispersion of hydrogen with a reservoir temperature of 50–64 K, using advanced laser diagnostics to accurately measure instantaneous hydrogen concentrations and particle image velocimetry to measure flow velocity. We have measured the 2-dimensional concentration fields and compared this to the Winters and Houf model [27, 28].

2. EXPERIMENTAL DESCRIPTION

Liquid hydrogen tanks store hydrogen at fairly low pressure (usually 3–5 bar), and at the saturated liquid temperature (28 K at 6 bar_{abs} and 23 K at 2 bar_{abs}). The cryogenic hydrogen release experiment was designed to simulate these conditions.

2.1. The cryogenic hydrogen release platform

Cryogenic hydrogen release experiments were performed at the Turbulent Combustion Laboratory at Sandia National Laboratories. A sketch of the cryogenic hydrogen release experimental system is shown in Fig. 2-1. During experiments, compressed gaseous hydrogen flowed into the laboratory first, the pressure of gaseous hydrogen was regulated by a Tescom 44-3200 series pressure regulator, and the flow rate of gaseous hydrogen was measured by a Teledyne-Hastings (HFM-D-301) mass flow meter. Then, hydrogen flowed back outside the lab and into a vacuum insulated three-stage heat exchanger (Meyer Tool & Mfg. Inc.). To monitor hydrogen temperatures inside the heat exchanger, silicon diode temperature sensors were installed at the inlet and exits of stages one and three. To monitor the height of cryogen baths, liquid level sensors were installed in the first and third stages of the heat exchanger. In the first stage of the heat exchanger, coiled stainless steel tubing was dipped inside a bath of liquid nitrogen and gaseous hydrogen inside the tubing was cooled to around 80 K. In the second stage, the gaseous hydrogen was further cooled in a counter-flow tube-in-tube heat exchanger by the cold gaseous

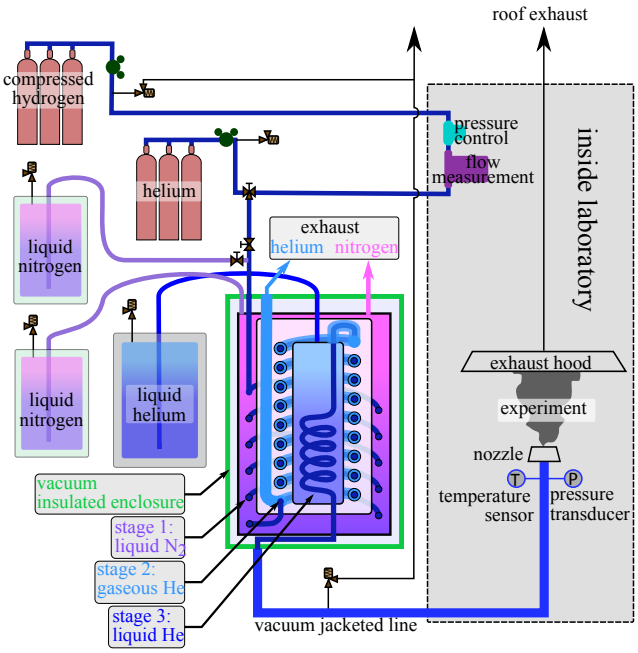

Figure 2-1 Sketch of the cryogenic hydrogen release experiment at the Turbulent Combustion Laboratory, Sandia National Laboratories.

Table 2-1 Cryogenic underexpanded hydrogen jet release experiment operating conditions.

Parameter	Range
Pressure (bar_{abs})	2.0 – 6.0
Temperature (K)	37 - 295
Diameter (mm)	0.75, 1.00, 1.25
H_2 mass flow rate (g/s)	0.1 - 0.7

helium generated from the third stage exhaust. Finally, the precooled gaseous hydrogen flowed through a bath of liquid helium where it was cooled down to the saturation temperature. The saturated hydrogen flowed through a vacuum jacketed line into the laboratory, and the exit conditions were monitored using a silicon diode temperature sensor and a pressure transducer (Omega PX 419-150GI) near the release point. The hydrogen was released in the lab through a small interchangeable orifice (0.75 mm, 1 mm and 1.25 mm diameter). All gases and products of combustion were collected by an active laboratory exhaust system and expelled outside. A three-way valve upstream of the heat exchanger allowed the user to switch between gaseous hydrogen and helium flowing through the experimental system. This valve allowed users to purge the lines, extinguish flames, and served as a safety feature of the experiment. If hydrogen was detected by one of several flammable gas sensors in the laboratory, this solenoid valve would switch, flowing helium through the heat exchanger, vacuum jacketed line, and nozzle. This active purge prevented the back-flow and freezing of air in the cold lines under an alarm condition. A LabVIEW program was used for data acquisition and experimental control.

2.2. Maximum ignition distance measurement

A systematic operating procedure was developed to operate the cryogenic release experiments. The heat exchanger tubing and the vacuum jacketed lines were first purged with gaseous helium, then pre-cooled with liquid nitrogen all the way up to the release point. In the meantime, the stage 1 bath was also filled with liquid nitrogen. Finally, when gaseous hydrogen started to flow, the heat exchanger was operated with liquid helium in stage 3, cooling hydrogen down to the saturation temperature. To achieve steady-state operation at a constant temperature below 50 K at the nozzle, approximately 3 h were required. During the cool down procedure, all the gaseous hydrogen was released inside the laboratory and vented through the active exhaust hood.

The experimental operating conditions for the under-expanded cryogenic hydrogen jets are summarized in Table 2-1. A laser spark ignition system was used to determine the maximum ignition distance of the cryogenic under-expanded hydrogen jets. An 8 mm beam from a Nd:YAG laser (9 ns pulse duration, 100 mJ/pulse, 532 nm wavelength) was focused using a spherical plano-convex lens ($f = 300$ mm), to form a plasma channel that was roughly 1 mm in diameter and 4 mm long. The centroid of the laser spark plasma channel was aligned to the jet centerline. Phuoc and White [30] have determined that, in this setting, the laser energy was sufficient to ignite the leanest or richest flammable hydrogen/air mixtures. At each spark location, up to 75

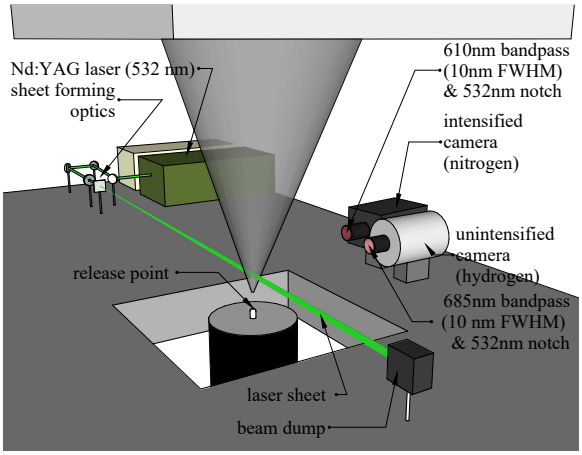

Figure 2-2 Diagnostic setup of experiment. A frequency doubled Nd:YAG laser is formed into a sheet, and Raman signals at two specific wavelengths are collected simultaneously by two cameras.

laser sparks were generated (5 s at 15 Hz). The hydrogen release apparatus was installed on a translation stage and was translated vertically until a sustained jet flame was established at the maximum ignition distance. The range of nozzle exit pressures was 2–6 bar, the temperature varied from 37 to 295 K, and the nozzle orifices were switched between a 0.75, 1.00 and 1.25 mm diameter. A total of 140 data points of maximum ignition height were collected across the range of pressure, temperature and nozzle exit diameters.

2.3. Raman scattering imaging of the cryogenic hydrogen releases

The cryogenic hydrogen release platform described in Section 2.1 was used to generate releases of ultra-cold hydrogen in the laboratory. In addition, to minimize the effect of any spurious room currents, the released hydrogen was surrounded by a co-flow of air through a 19 cm diameter honeycomb at 0.3 m/s. A sketch of the Raman scattering imaging setup is shown in Fig. 2-2. A 18 mm high laser sheet was generated using the same Nd:YAG laser with doubled frequency (532 nm, 9 ns pulse 700 mJ/pulse). The laser sheet was focused using a spherical plano-convex ($f = 1000$ mm) and a cylindrical plano-concave ($f = 200$ mm) lens pair. On one side of the cryogenic hydrogen releases, two cameras were set up to capture Raman scattered light from nitrogen and hydrogen. The nitrogen camera was an intensified PIMAX ICCD operated with a gain of 255 and cropped to approximately of the height. The hydrogen camera was an unintensified PIXIS 400B operated with 4x4 on-chip binning. The intensified nitrogen camera had its lenses slightly offset to focus the entire image plane using the Scheimpflug principle. Both cameras were outfitted with a Nikon 50 mm lens, a Nikon 3T close up lens, an OD 6, 532- nm, 17-nm FWHM notch filter to block out the laser light, and a stack of three OD 4 10 nm FWHM bandpass filters to filter out light except for the Stokes-shifted spontaneous Raman scattering from the desired gas molecules. The passband of nitrogen camera was centered at 610 nm to capture

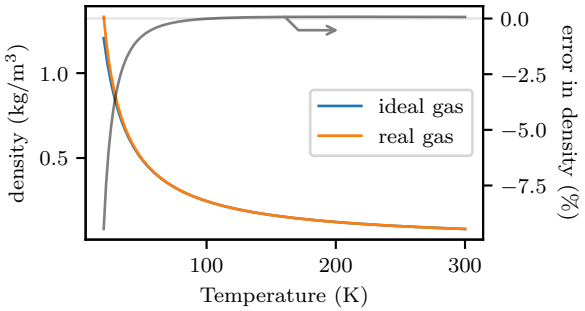

Figure 2-3 Density of hydrogen at atmospheric pressure (101325 Pa) calculated using a real gas equation of state [32] and the ideal gas law, as well as the error in density using the ideal gas law.

the Raman light at 607 nm, and the passband of hydrogen camera was centered at 685 nm to capture the Raman light at 683 nm.

2.3.1. Lens and camera calibrations

Spontaneous Raman shifted scattering is proportional to the concentration of each gas and the intensity of the incident laser light. The proportionality constant is a function of the cross-section of the gas molecules as well as the collection efficiency and response of the lens and camera systems. To linearize the response of the lens and camera systems, calibrations were first performed on each lens and camera system [31]. With the same optics in place, a pure flow of either hydrogen or nitrogen was generated, and Raman signals were collected. The signals were corrected for the laser sheet intensity by dividing by the average laser power in the horizontal direction. A functional fit was found to relate the signal counts to the intensity of light at each pixel location (binned, for the unintensified camera). Rather than using higher order polynomial to fit the response [31], a single proportionality constant was found for the small Raman signals detected in our case. This calibration method corrected the unequal response for each camera pixel (possibly binned), and vignetting that was observed towards the edges of each image.

Since we are not attempting to measure within the expansion zone of these releases. In this analysis, we assume that the releases are at atmospheric pressure, and the ideal gas law can be used to relate the concentration of the gases to the mole fraction and temperature. At downstream of hydrogen release where temperatures are greater than 47 K, the error is less than 1% under this assumption (Fig. 2-3). For near-liquid temperature regions of the flow, this assumption may cause a nearly 10% error. We also assume that the temperature dependent cross-section changes are negligible, which should be valid for the low-temperature flows in this work. Mathematically, the intensity of Raman light can therefore be represented by the equations

$$I_{H_2} = k_{H_2} I_0 \frac{x_{H_2}}{T} \tag{1}$$

$$I_{N_2} = k_{N_2} I_0 \frac{x_{N_2}}{T}, \tag{2}$$

where k_{H_2} or k_{N_2} is a proportionality constant for each camera and lens system that includes the cross-section of the gas molecule, the collection efficiency and response of the camera system. We also stipulate that the mole fractions of hydrogen and air must sum to one, or $x_{H_2} + 1.28x_{N2} = 1$, where the factor 1.28 comes from the fact that air is 78% nitrogen. Calibrations were performed to determine the proportionality constant for each camera to the gas of interest (H_2 or N_2). An area of pure hydrogen was generated in the lab using a laminar coflow box and Raman signals were collected by both cameras. The area of hydrogen was surrounded by a coflow of pure nitrogen, enabling signal differentiation between air and nitrogen. Because the signals were corrected to scale the intensity of pure air a value of 1, the calibration constant for nitrogen was found to be $k_{N_2} = 1.28 \cdot 295$ K. The calibration constant for hydrogen was found to be $k_{H_2} = 2.05 \cdot 295$ K. A target was imaged by both cameras and the known geometry of the target image was used to align both camera images and scale them to true spatial dimensions. There were approximately 1.7 (4×4 binned) pixels per mm for the unintensified (hydrogen) camera, and approximately 4.6 pixels per mm for the intensified (nitrogen) camera.

2.3.2. Background normalization

The signal detected by each camera is composed of the desired signal (directly scattered Raman light) and backgrounds, which contain electronic background (the cameras are biased so that zero light still has small number of counts), background room light, background scattered light (either scattered secondarily off condensed moisture in the flow or outside the wavelength of interest). To normalize for the electronic background and background room light, a set of background images were taken for all data sets (without significant difference between an image set taken with a lens cap on or without the laser on, i.e. the background room light was negligible). In image regions just above and below the laser sheet, the background scattered light was averaged in the vertical direction, and subtracted to correct for the background scattered light. Images were then corrected for the flat-field intensity. Images from the intensified camera (N_2) were then aligned and scaled to the unintensified camera pixel dimensions. The laser sheets are neither completely uniform in the vertical direction nor of the same intensity from shot-to-shot, so in an air region (44 mm wide), the corrected, flat nitrogen images were averaged in the horizontal direction, and both the air and hydrogen (background corrected) images were divided by the vertical array to normalize for the individual shot laser intensity and non-uniformity in the y-direction. These corrected images images are the signal I/I_0 in Eqs. 1 and 2. Corrected signals could then be converted to mole fractions and temperatures at each pixel.

3. RESULTS AND DISCUSSION

3.1. Mass flow rate

The mass flow rate of hydrogen was measured experimentally using HFM-D-3-1 mass flow meter as described in Section 2.1. The mass flow rate was also calculated using a real gas equation of state [32], assuming isentropic expansion from the measured nozzle pressure and temperature to the sonic choked flow velocity through the small orifice. A comparison between the experimentally measured and calculated mass flow rate of H_2 for all the test cases is shown in Fig. 3-1. For most of the conditions, the measured mass flow rate is the same as the calculated flow rate. There are some slight deviations at higher pressures and colder jet temperatures; no more than 10% error were observed for the conditions studied.

Ricou and Spalding [33] reported the mass flow rate for momentum dominated axisymmetric jets of non-uniform density. The entrained mass flow rate increases with distance from the nozzle exit, scaling inversely by the square root of the density of the jet at the nozzle. Using a developing entrainment coefficient, Han and Mungal [34] also observed a similar trend in the entrainment rate for turbulent reacting jets. The mass flow rate ($\dot{m}(x)$)at any point along the axis of the jet is given by

$$\frac{\dot{m}(x)}{\dot{m}_0} = C\frac{x}{D}\sqrt{\frac{\rho_\infty}{\rho_0}} \tag{3}$$

Where $\dot{m}_0$ is the initial mass flow rate (through the orifice), C is an entrainment constant (0.32 for non-reacting, isothermal jets), x is the distance from the release point along the jet axis, D is the nozzle diameter, ρ_∞ is the density of the entrained gas, and ρ_0 is the stagnation density of the released gas. The quantity $D\sqrt{\rho_\infty/\rho_0}$ is often called an effective diameter, D_{eff}, for an

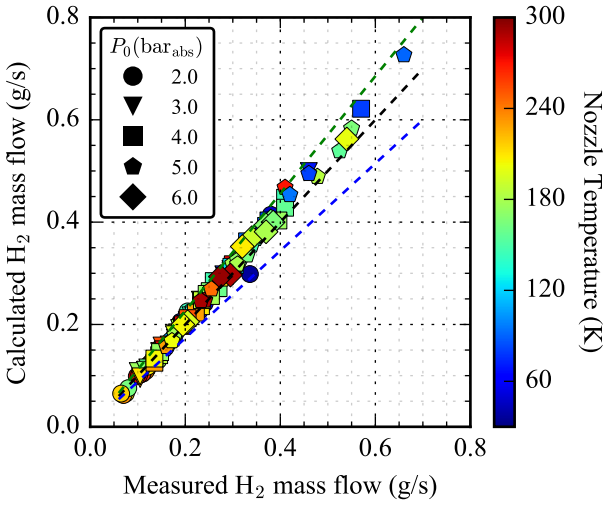

Figure 3-1 Calculated mass flow rate from the ignition experiments as a function of measured mass flow rate. Black dashed line is the 1:1 comparison, blue and green dashed lines show the $\pm$10% boundary.

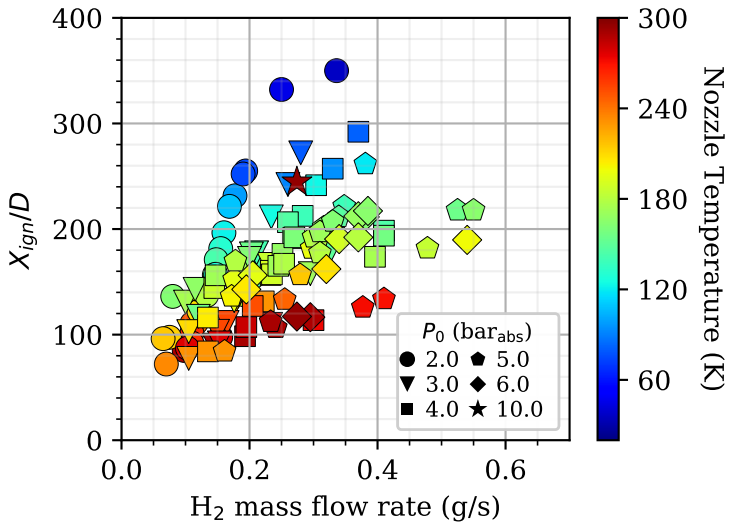

Figure 3-2 Maximum ignition distance as a function of mass flow rate for all the nozzle pressure, temperature and diameters studied.

under-expanded jet. The effective diameter is the diameter through which the jet mass flow rate would pass at atmospheric pressure to give the same momentum flux as the under-expanded jet at the nozzle exit. Li et al. [35], in a recent study of under-expanded hydrogen jets, confirmed that the variation of mean hydrogen mass fraction along the jet centerline depends on the effective diameter of the jet in the momentum dominated regime.

3.2. Maximum ignition distance

Depending on the local fuel mass fraction, an ignition kernel formed at a particular location could propagate towards the release source leading to a sustained jet flame [36, 37]. The maximum ignition distance (X_{ign}) depends on the hydrogen pressure, temperature, and leak diameter. The X_{ign} of under-expanded cryogenic hydrogen jets were measured at all the nozzle pressure temperature and diameter studied. Fig. 3-2 shows a scatter plot of the X_{ign} as a function of hydrogen mass flow rate. The symbols here represent the nozzle pressures and the color of the symbol denotes the hydrogen temperature at the release point. With the same mass flow rate of hydrogen, colder jets have a higher X_{ign}. In our studies, the X_{ign} was also found to scale with the effective diameter of the jet. Figure 3-3 shows the correlation between the X_{ign} and the effective diameter. Same as in Fig. 3-2, the symbols represent the pressure and the color represents the temperature at the nozzle. The scatter plot of the X_{ign} for all the test cases fits into a linear dependence on the effective diameter (the black dashed line Fig. 3-3). Friedrich et al. [29] also reported that the X_{ign} for cryogenic hydrogen jets can be expressed by $X_{ign} = 0.639D\sqrt{\rho_0/\rho_\infty}$ (the blue dashed line in Fig. 3-3). The operating conditions and the X_{ign}s reported by other groups [36, 38, 39] are shown in Table 3-1. It is unclear why this correlation from Friedrich et

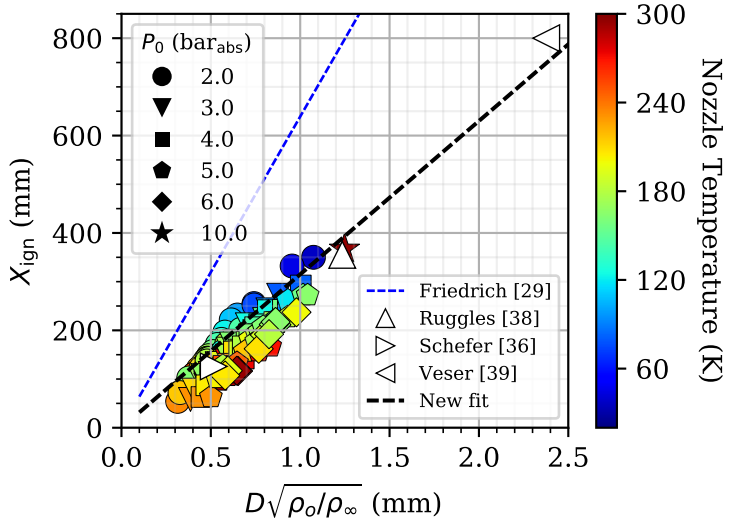

Figure 3-3 Maximum ignition distance as a function of effective diameter, for the cryogenic hydrogen releases in the current study and data from the literature. Blue dashed line shows a correlation from Friedrich et al. [29] and the green dashed line is a modified correlation proposed in this work.

Table 3-1 Operating conditions and the maximum ignition height reported by different research groups.

Literature Source	T (K)	P (bar)	D (mm)	X_{ign} (mm)
Schefer et al. [36]	295	1.0	1.91	126
Ruggles et al. [38]	295	9.89	1.5	365
Veser et al. [39]	290	5	4	800

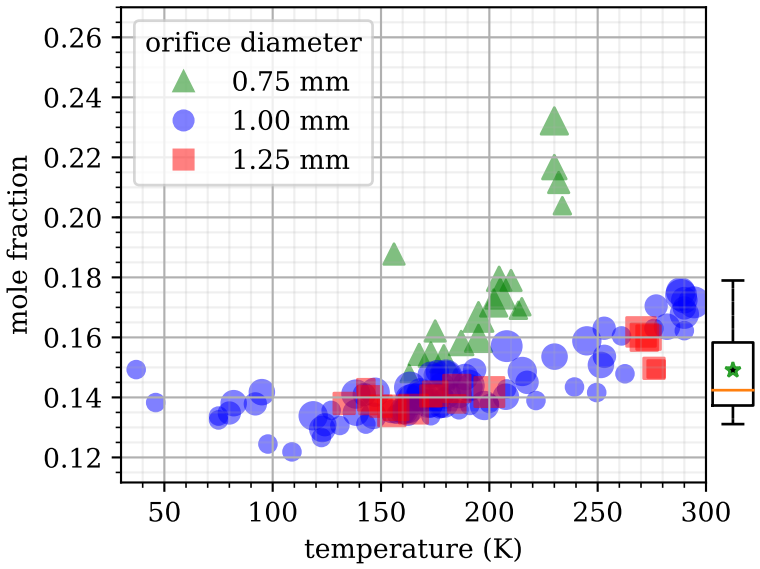

Figure 3-4 Simulated jet mean hydrogen mole fraction at each ignition point. Points are sized by pressure. Box plot to right of axes shows the median mole fraction (line), quartiles (box edges), 5 and 95% of the data (whiskers), as well as the mean value (star).

al. [29] is so conservative, over-predicting the X_{ign} for the conditions from the current experimental data as well as other reported data [36, 38, 39]. In Friedrich's work, the key differences are that an intrusive jet engine electrical ignitor was used and the jets were oriented horizontally. While there may have been some flame stabilization on the ignitor, flow disruption from the ignitor, and buoyancy influence on flame propagation, it is unlikely that these effects would lead to the nearly factor of two difference in X_{ign}. A new correlation shown in the plot is a good fit for current data set as well as the reported values in other work [36, 38, 39], given by

$$X_{ign} = 0.430 D \sqrt{\frac{\rho}{\rho_\infty}} \tag{4}$$

Houf and Winters developed a model for a high-momentum, cryogenic hydrogen release [28]. The conditions in the experiment were simulated using this model (neglecting zone 2), and the hydrogen mole fraction at X_{ign} was extracted from the simulations. The extracted mole fraction at the X_{ign} is plotted as a function of the release temperature in Fig. 3-4. There does not seem to be a significant correlation with temperature (perhaps a slight increase in mole fraction as the release gas warms) or pressure (shown by the size of the symbols). As shown by the box plot to the right of the axes, 90% of the data falls between a mole fraction of 0.13 and 0.18, with the majority of the outliers towards the higher mole fractions, and, with the 0.75 mm orifice giving the highest calculated mole fractions at the ignition point. Schlieren imaging showed some vertical deviation for the 0.75 mm orifice, indicating that the ignition point is likely not along the centerline for these releases. An off-axis ignition would occur closer to the release point than an on-axis ignition, leading to a higher calculated mole fraction along the centerline. In their studies, the mean calculated mole fraction at the ignition point is 0.149, while the median is 0.142, and the

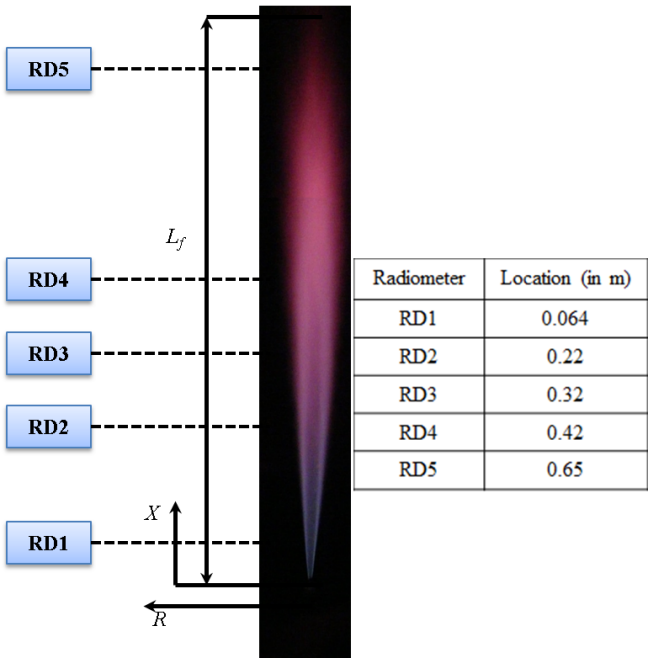

Radiometer	Location (in m)
RD1	0.064
RD2	0.22
RD3	0.32
RD4	0.42
RD5	0.65

Figure 3-5 Schematic of the location of the radiometer with respect to an under-expanded jet flame.

minimum calculated mole fraction at the ignition point is 0.122. All of these values are higher than the 11% boundary, which is observed by Veser et al. [39] for the fast flame regime of horizontal 80 K hydrogen releases. One potential reason for the higher mole fraction could be buoyancy effects from these vertical jets, as compared to the horizontal jets of Veser et al. [39]. A mean mole fraction above the 4% lower flammability limit of hydrogen is required to ignite turbulent jets because there are pockets of rich and lean concentrations flowing by the ignition point, and the flame speed in the lean pockets needs to overcome the momentum of the flow. It should be cautioned that the model used to calculate the mole fractions in Fig. 3-4 was not not previously validated for cryogenic hydrogen releases. Validation of the model is discussed in Section 4.

3.3. Flame property measurements: radiant power, length and width

The thermal radiation from a jet flame poses potential threats to the safety of people and infrastructure. For the development of hydrogen safety codes and standards, radiative heat flux is a key aspect of flames that needs to be investigated. To characterize the thermo-physical properties of an ignited under-expanded cryogenic hydrogen jet, the incident radiative power was measured by five 150° view angle Schmidt-Boelter thermopile detectors (Medtherm Model 64P-1-22). A ZnSe window on the face of each detector has 70% transmission between 0.7 and 17 μm. As shown in Fig. 3-5, the thermopile detectors were installed at five different locations along the length of the jet flame, and radially 8 inches (20 cm) away from the jet axis. Detector

measurements were recorded over 1 min and the averaged data were calculated as the radiative heat flux. To scale the radiative heat flux from a jet flame, two factors are needed: the flame length (L_f) and flame width (W_f). Visible and IR flame images were recorded to calculate L_f and W_f. The IR images were recorded by a FLUKE TI 400 camera with transmission in the range of 7.5–14 μm IR spectral bands. The visible flame images were captured by a commercial Panasonic Lumix camera.

3.4. The flame length and width

For both subsonic and under-expanded jet flames, Kalghatgi's group [40] has measured L_f. Their measurements showed a linear dependence of L_f on the mass flow rate. They also determined that a flame grows with nozzle diameter at a fixed mass flow rate. More recently, Friedrich et al. [29] also reported that at cryogenic temperatures of 34–65 K and pressures of 7-30 bars, the measured heat flux scales with the hydrogen mass flow rate. However, these data did not demonstrate the dependence of the flame length or the radiative heat flux on the release temperature of the under-expanded hydrogen jets. In the current study, the effect of the hydrogen temperature at the nozzle on the radiative properties of the jet flame was quantified by systematically varying it from room temperature (295 K) to near the saturation temperature (37 K). Figure 3-6 shows the comparison of the averaged IR image and visible image of a cryogenic hydrogen jet flame released with a 1 mm diameter nozzle at 2 bar and 55 K. The flame is vertically oriented with the nozzle center at $r = 0$ mm and $x = 0$ mm of the image. The field of view for the IR camera was 0.28 m; the vertical stage was traversed in steps of 0.2 m; a series of five IR images were averaged at every location to construct the entire flame length. The flame length was determined using the distance from the nozzle exit (along the axis of the flame) where the intensity drops to 10% of the maximum intensity level for that image. Reported flame length and width are the average of the IR and visible values. Figure 3-7 shows the calculated flame length as a function of hydrogen mass flow rate. Consistent with recent reports [29, 40], there is an increase in the flame height with hydrogen mass flow rate. Moreover, it is clear that the flame length increases with a decrease in nozzle temperature for a fixed mass flow rate. Several reported methods [41, 42] were tested to define the correlation of our findings in flame length and mass flow rate.

Schefer et al. [41] studied hydrogen diffusion flames and defined a dimensionless flame length, L^*,

$$L^* = L_f \frac{f_s}{D_{eff}} \tag{5}$$

where L_f is the measured flame length, f_s is the stoichiometric mass fraction and D_{eff} is the effective diameter (same as defined in Section 3.1). The dimensionless flame length was shown to be dependent on the flame Froude number, which is defined as:

$$\mathrm{Fr}_f = \frac{V_j f_s^{3/2}}{\left(\frac{\rho_e}{\rho_\infty}\right)^{1/4} \sqrt{\frac{gD\Delta T_f}{T_\infty}}} \tag{6}$$

where, ρ_e/ρ_∞ is the ratio of jet gas density to ambient gas density, and ΔT_f is the peak flame temperature rise due to combustion heat release.

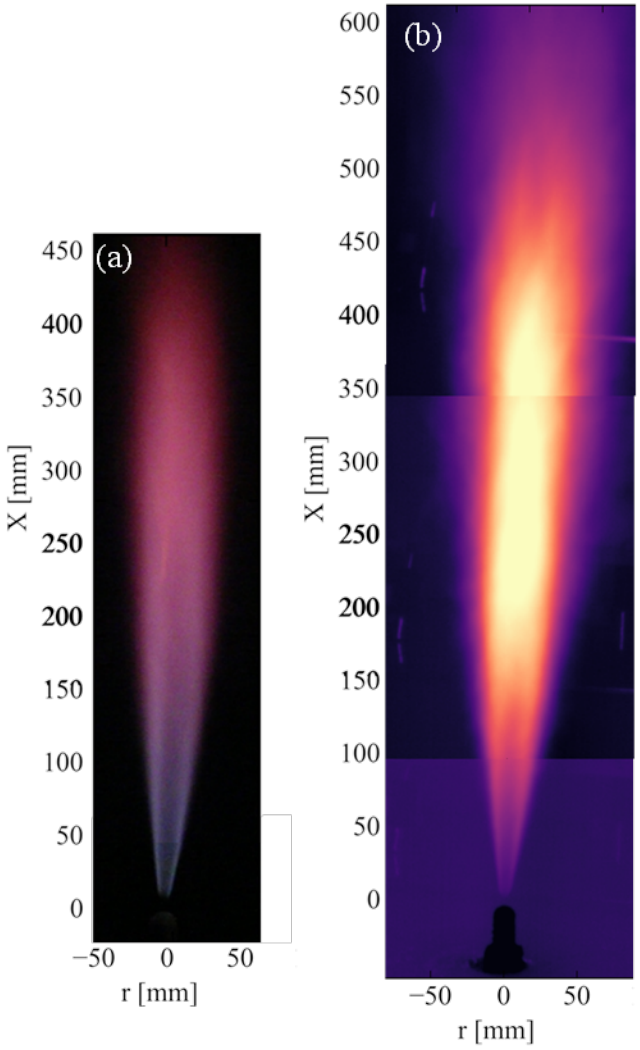

Figure 3-6 (a) Visible and (b) IR flame image for a cryogenic under-expanded hydrogen flame. Source is a 1 mm diameter nozzle at 2 bar$_{abs}$ and 55 K.

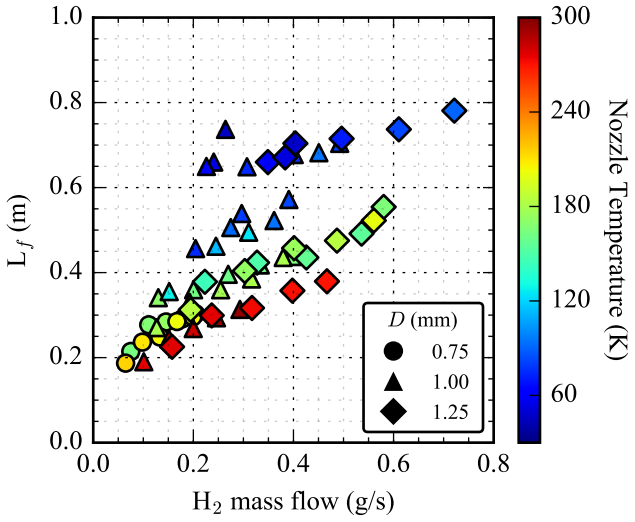

Figure 3-7 Flame length as a function of mass flow rate.

Based on Schefer et al.'s equations [41], all the flames in this study should have a $L^* = 23$. Figure 3-8 shows the comparison of the dimensionless flame lengths measured in this study and reported by different authors. Our data showed a large scatter around the $L^* = 23$ line (gray line in Fig. 3-8), with a range of $15 \leq L^* \leq 30$. No linear correlation was observed.

Molkov and Saffers [42] also reported this scatter when comparing the flame lengths from a wider range of experimental data [40, 41, 43–46]. Based on a similar analysis to correlate flame length with flow (i.e, density, velocity, viscosity) and geometric variable (i.e, diameter), Molkov and Saffers [42] expressed flame length differently than Schefer et al. [41], as a function of mass flow rate, $\dot{m}$, diameter, D, and jet viscosity, μ_N, as

$$L_f = f\sqrt{\frac{4\dot{m}D}{\pi\mu_N}} = fD\sqrt{\mathrm{Re}} \tag{7}$$

Since Molkov and Saffers' equation was defined for atmospheric temperature hydrogen releases, the lack of variations in viscosity allowed the flame length to be shown to scale as, $\sqrt{\dot{m}D}$.

For the cryogenic hydrogen jet flames in this study, using similar scaling analysis discussed by Molkov and Saffers [42], we express a normalized flame length, L_f/D, as a function of the square root of the Reynolds number, Re (based on the throat density, viscosity, choked flow velocity, and diameter). Figure 3-9 shows the variation of L_f/D from the current study, along with the previously reported data [40, 41, 43, 44, 46, 47]. The data collapses on to a line with the equation of the best fit given by

$$\frac{L_f}{D} = 0.86\sqrt{\mathrm{Re}} \tag{8}$$

The increased scatter at larger Reynolds numbers could be due to larger turbulent fluctuations, leading to increased experimental uncertainty in measuring flame length.

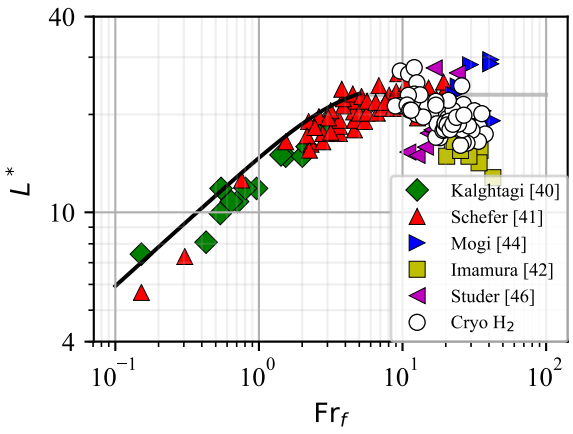

Figure 3-8 Variation of dimensionless flame length, L^*, as a function of Froude number, for the cryogenic hydrogen releases for the current study, along with data from literature.

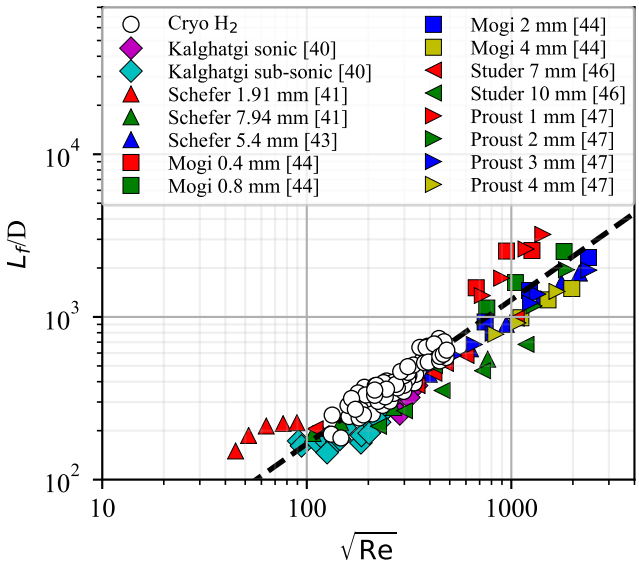

Figure 3-9 Variation of flame length, L_f, as a function of Reynolds number, for the cryogenic hydrogen releases for the current study, along with data from the literature.

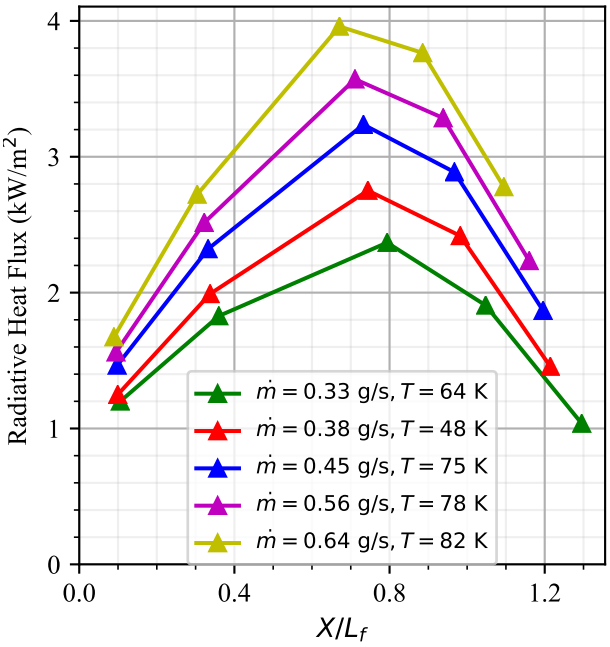

Figure 3-10 Radiative heat flux along the length of the jet flame, for several cold release conditions.

3.5. The radiative heat flux

The radiative heat flux for five different cryogenic hydrogen releases was also measured in this study. Figure 3-10 shows the axial variation of the radiative heat flux. The axial locations (X) of the radiometers are normalized by the respective measured flame length, and the peak value in the radiative heat flux is observed at X/L_f in the range of 0.7–0.8 (Fig. 3-10). This is an expected behavior for a turbulent jet flame [48]. It is also noticeable that with an increase in H_2 mass flow rate ($\dot{m}$), there is a corresponding increase in the peak value of the radiative heat flux, regardless of the release temperature.

Figure 3-11 shows the variation of radiative heat flux as a function of hydrogen mass flow rate. There is an increase in the heat flux with an increase in hydrogen mass flow rate. Moreover, for a fixed mass flow rate of hydrogen, the radiative heat flux increases with colder jet releases and larger nozzle diameter.

Table 3-2 summarizes the maximum ignition distance and maximum heat flux measured at 25 representative operating conditions. The stagnation density, nozzle density and speed of sound is calculated using the real gas equation of state [32, 49].

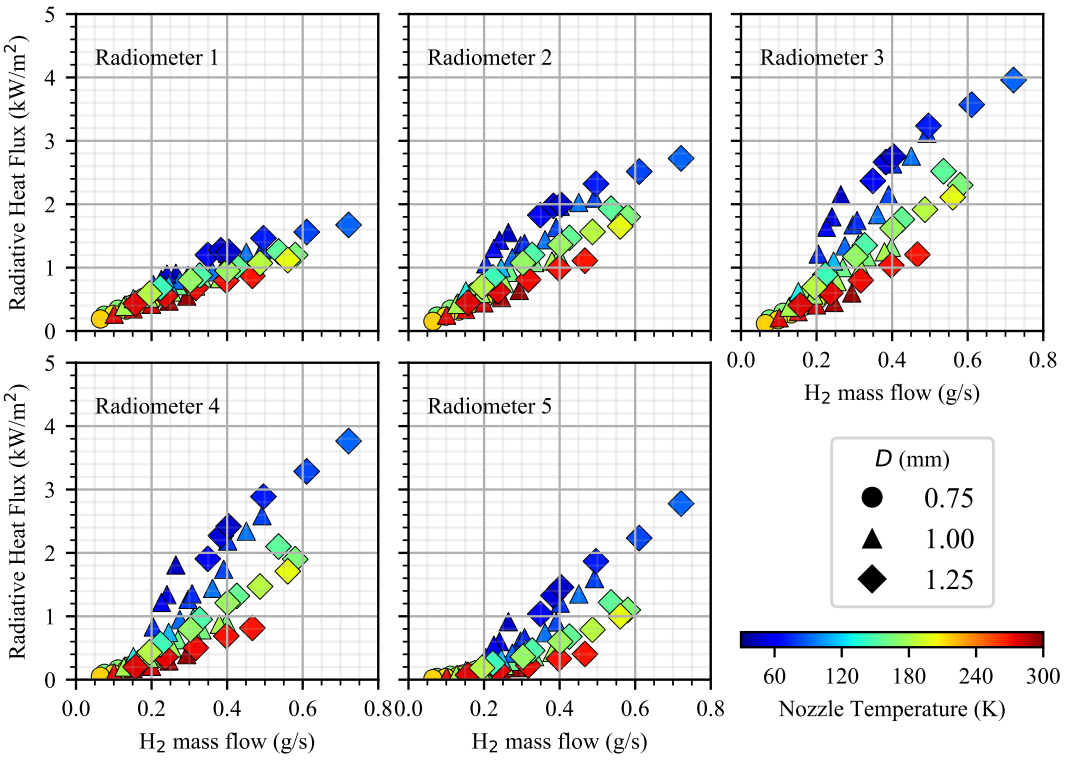

Figure 3-11 Radiative heat flux measured by each of the radiometers for all the test conditions.

Table 3-2 Cryogenic under-expanded hydrogen jet release experimental parameters and measured quantities.

TEST ID	D (mm)	P (bar)	T (K)	$\dot{m}$ (g/s)	ρ_0 (kg/m^3)	X_{ign} (mm)	L_f (m)	Peak Q_{rad} (kW/m^2)
1	0.75	2	163	0.08	0.3	102.2	0.215	0.19
2	0.75	5	179	0.178	0.68	127.2	0.292	0.57
3	0.75	6	205	0.195	0.71	107.2	0.296	0.48
4	0.75	2	215	0.065	0.23	72.2	0.187	0.12
5	1	2	46	0.25	1.08	332.2	0.737	2.15
6	1	2	55	0.241	0.89	321.2	0.66	1.8
7	1	2	62	0.23	0.79	307.2	0.65	1.64
8	1	4	78	0.375	1.25	307.2	0.678	2.64
9	1	5	81	0.46	1.51	332.2	0.704	3.12
10	1	3	113	0.24	0.64	227.2	0.462	1.1
11	1	4	124	0.297	0.78	227.2	0.495	1.37
12	1	2	129	0.147	0.38	157.2	0.355	0.62
13	1	3	162.5	0.2	0.45	172.2	0.36	0.68
14	1	3	175	0.195	0.41	147.2	0.33	0.57
15	1	6	294.5	0.274	0.49	117.2	0.314	0.6
16	1.25	2	48	0.38	1.08	412.2	0.704	2.75
17	1.25	2	53	0.365	0.93	387.2	0.671	2.66
18	1.25	2	64	0.33	0.76	372.2	0.66	2.37
19	1.25	3	70	0.46	1.05	392.2	0.715	3.24
20	1.25	5	90.7	0.66	1.34	397.2	0.781	3.96
21	1.25	2	144	0.213	0.34	202.2	0.378	0.89
22	1.25	5	155	0.525	0.78	272.2	0.492	2.52
23	1.25	2	185	0.192	0.26	172.2	0.312	0.69
24	1.25	6	200	0.54	0.72	237.2	0.523	2.11
25	1.25	5	271.5	0.377	0.45	157.2	0.358	1.04

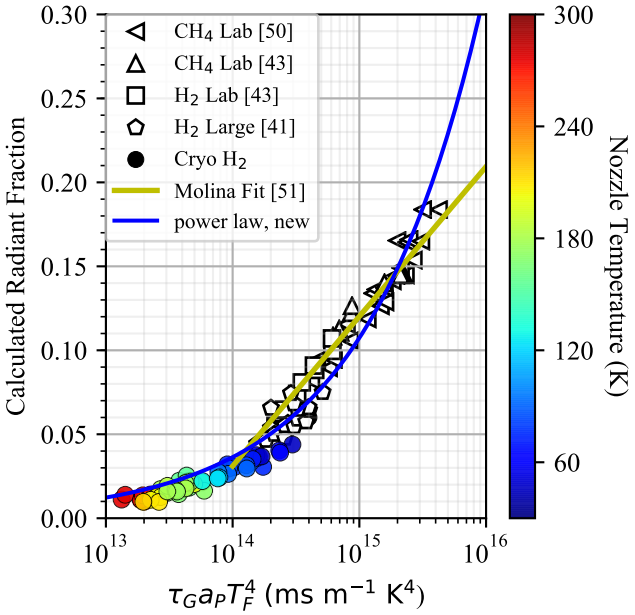

Figure 3-12 Radiant fractions for the cryogenic hydrogen jet flames.

3.6. The radiant fraction

In a scaling analysis, Turns and Myer [50] proposed that the radiant fraction, χ_r, from a non-premixed turbulent jet flame can be scaled as a function of

$$\chi_r = \frac{S_{rad}}{\dot{m}\Delta H_c} \propto \frac{a_P T_f^4 D}{V_j} \tag{9}$$

where S_{rad} is the total radiative power emitted from the flame, ΔH_c is the heat of combustion, a_P is the Planck-mean absorption coefficient for an optically thin flame, T_f is the adiabatic flame temperature, V_j is the jet exit velocity and D/V_j is the flame residence time. The Planck-mean absorption coefficients for the different flames (0.23 for hydrogen) are based on the RADCAL calculations reported by Molina et al. [51]. A global flame residence time in terms of the flame geometric parameters and fluid properties was also defined as

$$\tau_G = \frac{\rho_f W_f^2 L_f f_s}{3\rho_0 D^2 V_j} \tag{10}$$

The radiative fraction for a momentum dominated flame was found to be proportional to the $\log(\tau_G)$, as shown in Fig. 3-12, where χ_r is plotted as a function of $a_P \tau_G T_f^4$. The data from the current study is compared with the literature data for hydrogen (H_2) and methane (CH_4) flames [41, 43, 50, 51] (Fig. 3-12). The majority of the flame residence times of the cryogenic hydrogen jet flames studied here are smaller than the under-expanded and lab scale hydrogen jet flames observed previously. Nonetheless, a trend continues into this region. This trend is different than the logarithmic correlation that the data previously suggested (yellow line in Fig. 3-12) [41,

50, 51]. A correlation based on power-law is proposed to predict the radiative fraction as a function of global flame residence time, given as

$$\chi_r = 9.45 \times 10^{-9} \left(a_p \tau_G T_f^4\right)^{0.47} \tag{11}$$

Now focusing on the radiant fraction data from the current study, the highest radiant fractions are seen for the lowest temperature releases. The speed of sound decreases as the temperature decreases. The nozzle exit velocity is equal to the speed of sound for all the choked, under-expanded jet flames studied herein. As shown in Eq. 11, as the velocity decreases, the global residence time increases, and there is a corresponding increase in the radiant fraction. This is an important finding with respect to the safety associated with cryogenic hydrogen infrastructure. The increased radiant fraction and total radiative power from these cryogenic releases over room temperature releases must be accounted for in the analysis of these systems.

4. RAMAN SCATTERING IMAGE OF CRYOGENIC HYDROGEN RELEASES

Raman scattering image sets were taken using method described in Section 2.3. Detailed experimental conditions are listed in Table 4-1. The mole fraction profiles of hydrogen/nitrogen and temperature for releases are shown in Fig. 4-1. The nozzle height was controlled vertically by adjusting the height of the translation stage. Each 10 mm increment was defined as a 1 nozzle height. The images of 400 individual laser pulses at each of 5 and 6 nozzle heights were taken by two cameras. The images at each height were stitched together to give the overall median profiles (the left and right frames in Fig. 4-1). This stitching is fairly smooth, being the least smooth towards the tops of the images. This is likely due to the fact that in the presumed air region at the far right 44 mm of the images, there may still be some hydrogen in this region. Moreover, the amount of humid air entrained, and hence, background scattered light, is also higher further away from the nozzle, causing more noise towards the tops of these images. On average, at 40 mm downstream from the nozzle, both the 3 and 5 bar jets have warmed around 50 K and the concentration of hydrogen has decayed by approximately 30%. The middle frame in Fig. 4-1 shows the stitched images of a single laser pulse at each of 5 and 6 nozzle heights. These images contain significantly more noise than the median images on the left and right. However, these individual images show that these jets are in fact turbulent, with eddies of varying mole fraction and temperature. Comparing the individual mole fractions and temperatures in the middle images to these in the median images (Fig. 4-1, left and right frames), regions of the flow with higher or lower hydrogen mole fractions were identified. Due to the turbulence, temperatures at a given location in the individual images are lower than the median temperature.

Table 4-1 Experimental conditions in this work.

T_{noz} (K)	P_{noz} (bar_{abs})	d_{noz} (mm)	$n_{heights}$	T_{throat} (K)	P_{throat} (bar_{abs})	ρ_{throat}	v_{throat} (m/s)
58	2.0	1.0	4	43.5	0.972	0.55	544.5
56	3.0	1.0	4	41.9	1.457	0.86	533.3
53	4.0	1.0	4	39.6	1.940	1.22	516.4
50	5.0	1.0	5	37.4	2.422	1.65	498.2
61	2.0	1.25	6	45.7	0.973	0.52	558.9
51	2.5	1.25	2	38.2	1.215	0.79	508.4
51	3.0	1.25	6	38.2	1.457	0.95	507.5
55	3.5	1.25	3	41.2	1.699	1.03	527.6
54	4.0	1.25	2	40.4	1.940	1.20	521.6

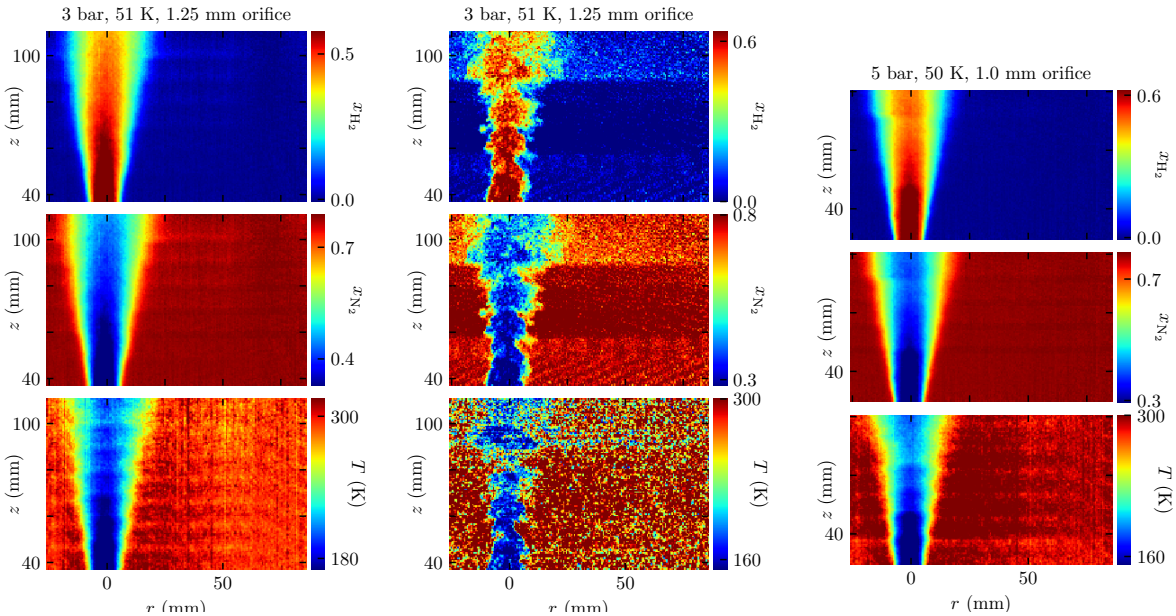

Figure 4-1 Profiles for mole fraction hydrogen (top frames), mole fraction nitrogen (middle frames), and temperature (bottom frames) for releases from a 1.25 mm orifice (left and center) and a 1 mm orifice (right). Left and right image sets are median values from 400 images. Central is an analyzed image set for a single laser pulse at each imaging height.

4.1. The variation in the nozzle pressure and temperature, hydrogen centerline mole fraction and temperature

The variation in nozzle pressure and temperature was also examined in this study (Fig. 4-2 left frames). 400 images were taken at each of 4–6 nozzle heights from the 1 mm nozzle. The pressure, being controlled by a pressure transducer, shows very little variation at 2, 3, 4, and 5 bar_{abs}. The temperature on the other hand, does have some variation, especially for the 5 bar_{abs} release. For the 5 bar_{abs} release, there is variation not only for each image set, but also at the different heights of the camera. The temperature varied by around 2° when the camera was approximately 40 mm from the nozzle, and by an average of 4° going from 40 mm to 80 mm. The density of 48 K hydrogen is nearly 10% higher than 52 K hydrogen, with a 5% lower choked flow velocity. This unsteadiness in the mass flow rate adds errors to the data, in addition to the errors associated with the noise on the cameras and the data processing techniques.

Similar to Fig. 4-2, the left frame in Fig. 4-3 shows the nozzle pressure, temperature, and centerline mole fraction and temperature for the experiments with the 1.25 mm diameter nozzle. The nozzle pressure was quite steady while there was up to 3° variation in nozzle temperature.

4.2. The variation in hydrogen centerline mole fraction and temperature

The right frames of Fig. 4-2 show the median centerline hydrogen mole fraction and temperature as a function of the distance from the 1 mm nozzle. The maximum hydrogen mole fraction and minimum temperature were observed to move laterally for some image sets, likely due to ice buildup near the nozzle. Rather than extracting the value of the mole fraction and temperature at the horizontal location 0 (see Fig. 4-1), the centerline temperature and hydrogen mole fraction in Fig. 4-2 are the maximum average mole fraction or minimum average temperature at each height over the horizontal distance of 0–90 mm. This change in extraction minimized the variation in the data where the different image sets were stitched together. Even with this modification of the centerline temperature or mole fraction, there are still some discontinuities observed in the centerline mole fraction at 4 bar, 50 mm and 5 bar, 85 mm. These discontinuities are even more obvious in the centerline temperature. Nonetheless, the trend in the centerline data is as expected, with decreasing mole fraction and increasing temperatures. The 2, 3, and 4 bar releases have very similar centerline mole fractions and temperatures, while the 5 bar release has the lowest temperature and highest centerline mole fraction. The shaded regions show the 25^{th} and 75^{th} quartiles of the mole fraction and temperature data. Some of these variations are due to noise on the data, but the majority of this spread is due to turbulent fluctuations in the flow.

Compared to 5h3 1 mm nozzle, there is a clearer trend in the centerline data for 1.25 mm nozzle, with decreasing mole fraction and increasing temperatures (Fig. 4-3, right frame). The increases in temperature and mole fraction variation moving downstream of the flow are more obvious.

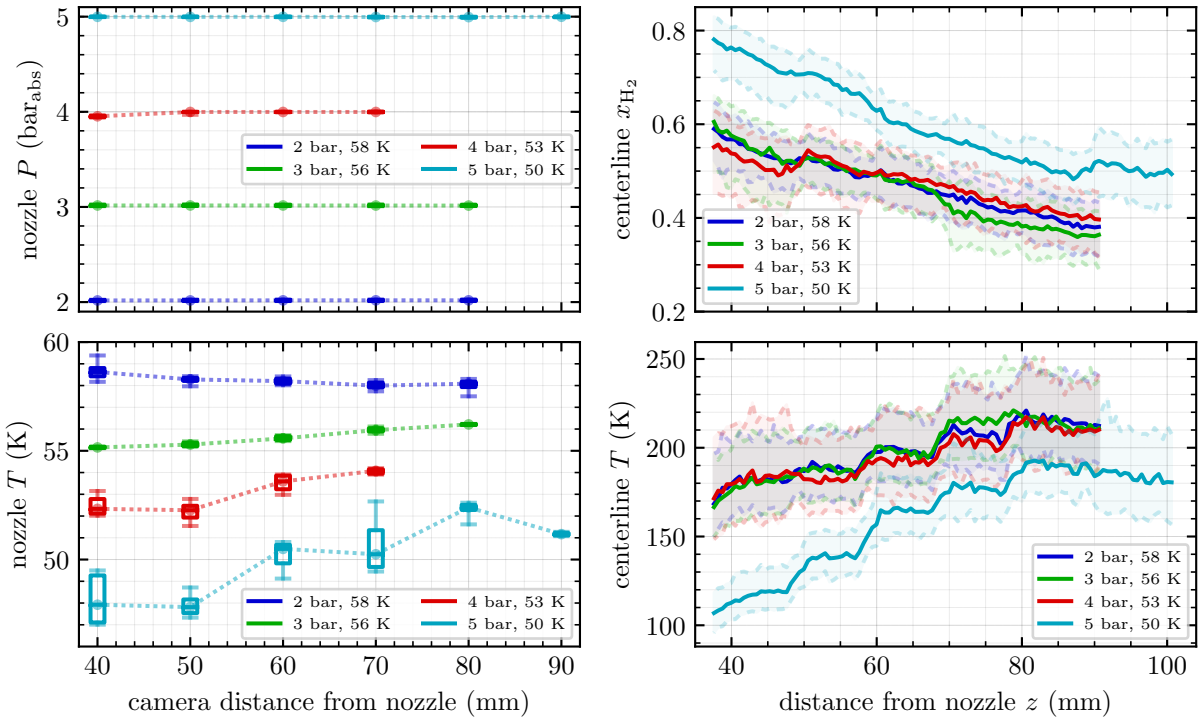

Figure 4-2 Nozzle pressure and temperature during data collection (left frames), and median centerline mole fraction and temperature (right frames) as a function of the distance from the nozzle, for the 1 mm orifice. In the left hand frames, the dashed line connects the median values while capturing images at each camera height, the boxes are the 25th and 75th quartiles, and the whiskers extend to the 5th and 95th percentage of the data. In the right-hand frames, the median centerline mole fraction or temperature are shown by the solid lines, while the shading proceeds out to dashed lines that capture the 25th and 75th quartiles of the data.

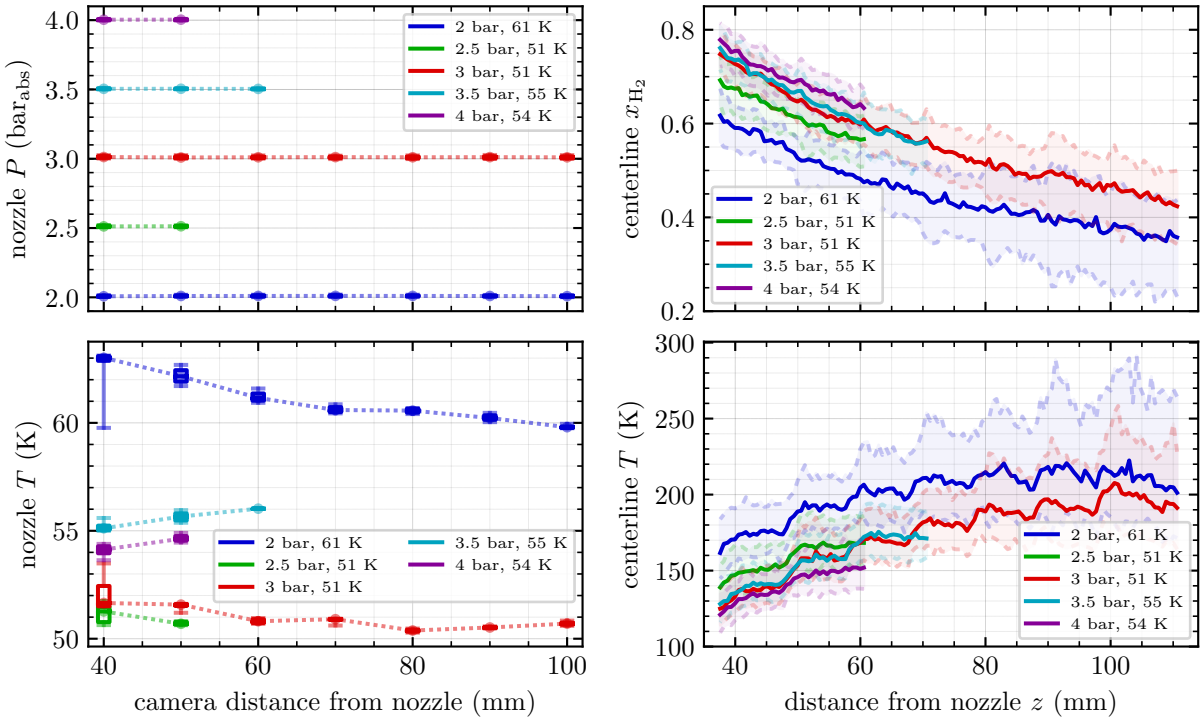

Figure 4-3 Nozzle pressure and temperature during data collection (left frames), and median centerline mole fraction and temperature (right frames) as a function of the distance from the nozzle, for the 1.25 mm orifice. In the left hand frames, the dashed line connects the median values while capturing images at each camera height, the boxes are the 25th and 75th quartiles, and the whiskers extend to the 5th and 95th percentage of the data. In the right-hand frames, the median centerline mole fraction or temperature are shown by the solid lines, while the shading proceeds out to dashed lines that capture the 25th and 75th quartiles of the data.

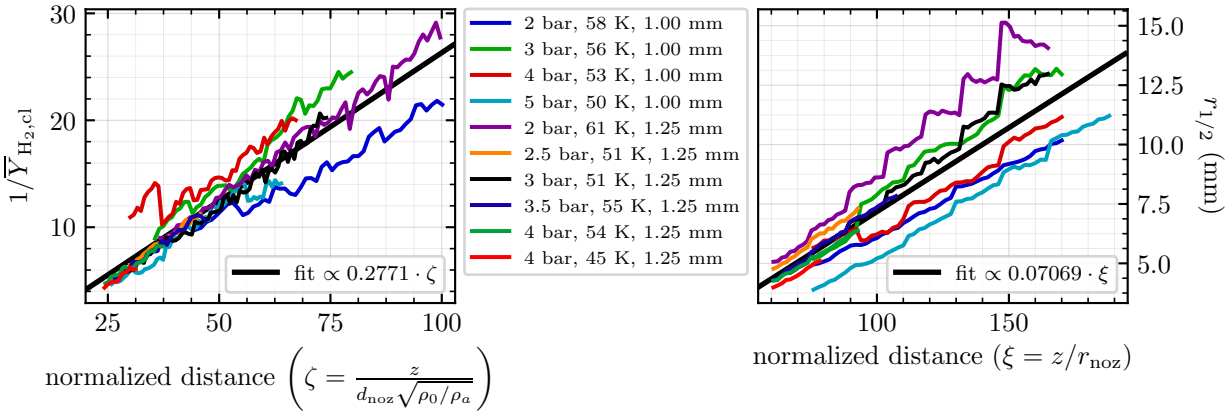

Figure 4-4 Centerline average inverse mass fraction decay (right) and mass fraction half-width (right) plotted as a function of the normalized downstream distance.

4.3. Mass fraction decay constant and half width decay rate

To determine the mass fraction decay constant, the downstream distance is normalized using the effective diameter, $d\sqrt{\rho_0/\rho_a}$, where d is the nozzle diameter, ρ_0 is the nozzle stagnation density, and ρ_a is the density of the room air. The normalized distance is linearly corelated to the decay of the inverse average mass fraction at the release centerline, with a constant of 0.277 (Fig. 4-4, left frame).

Other researchers [38, 52, 53] have reported the decay constant between 0.21 - 0.271 for room-temperature releases. Our proportionality constant of 0.277 is near this range, implying that the centerline mass fraction is decaying at a similar rate for a cryogenic release to a room-temperature release. In contrast, Friedrich et al. [29] reported a slower decay rate, which is likely due to errors in their sparse, extractive concentration measurements. Although it is possible that the slightly lower temperatures of those experiments cause the elucidation of a different phenomena, such as a greater effect from the phase change of the components in air.

The right frame of Fig. 4-4 shows the jet half-width ($r_{1/2}$) plotted as a function of the normalized distance. The half-width was found by fitting a Gaussian curve to each z pixel (each mm of height). The data collapses fairly well against this normalized distance. The slope of the best-fit line for all the data is 0.071 mm. While for room temperature jets, this half-width decay rate has been reported as a bit faster–around 0.1–0.11 [38, 52, 53].

Our observations in decay rate and half-width decay rate would suggest that the velocity decay along the centerline will be slower for cryogenic hydrogen than for warmer hydrogen. This will likely impact two empirical parameters in the model for these flows. First, the parameter that describes the ratio of the spreading of the velocity to the spreading of the concentration. The second is the empirically derived air entrainment rate–this may be a function of temperature, differentiating them from room temperature jets.

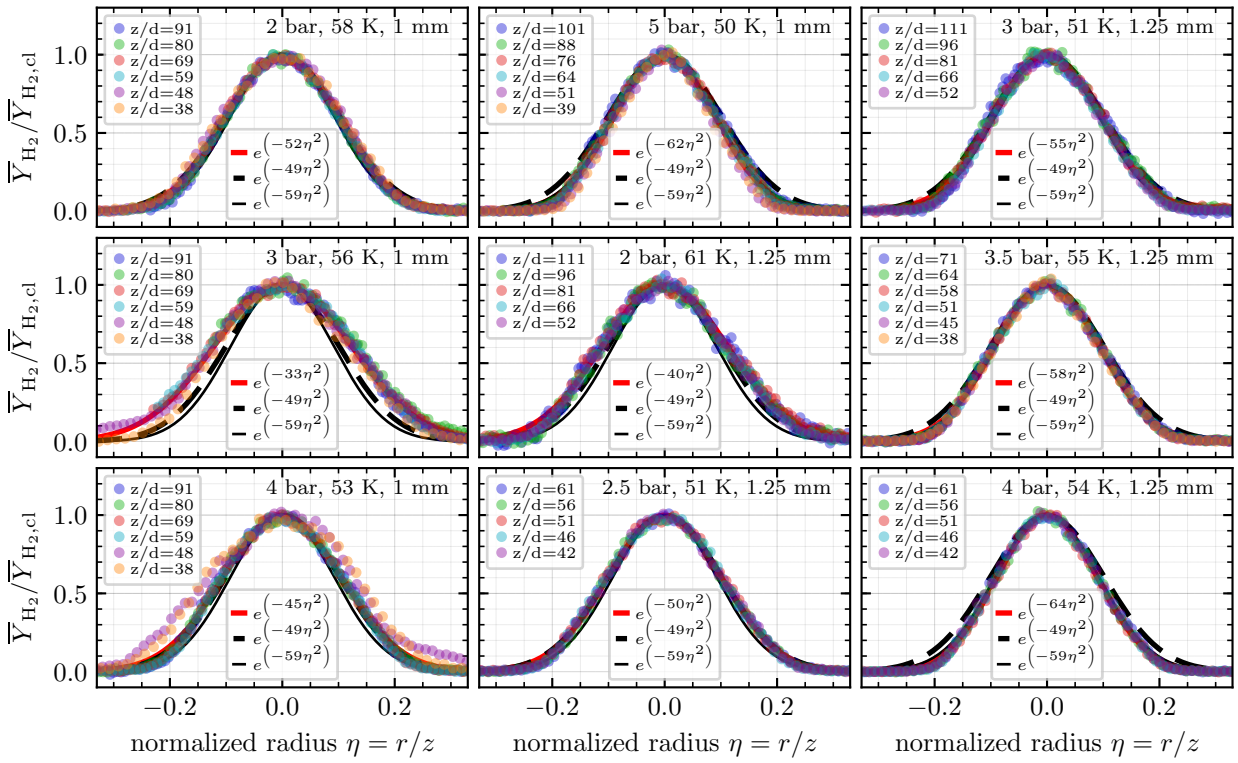

Figure 4-5 Radial mass fractions at selected distances, normalized by the centerline mass fraction. Three fits are shown on the graph. The red line is the fit for each condition (at all heights, not just the selected), the dashed thick black line is the fit for all 9 release conditions, and the thin black line is the literature fit [37, 38, 52].

Figure 4-5 shows the normalized hydrogen mass fraction as a function of the normalized radius for all the release conditions. The data collapses well using the normalization parameters of the average centerline hydrogen mass fraction, $\overline{Y}_{cl}$ and the downstream distance, z. The red line in each plot is the Gaussian fit for the release conditions of each frame (at all heights, not just the selected heights in the legend). The 4 bar, 54 K, 1.25 mm diameter nozzle release is the most narrow, with a fit of $\overline{Y}/\overline{Y}_{cl} = \exp(-64\eta^2)$, while the 3 bar, 56 K, 1 mm diameter nozzle release is the widest, with a fit of $\overline{Y}/\overline{Y}_{cl} = \exp(-33\eta^2)$. The thick dashed black line is the second Gaussian fit for all the different release conditions. In some frames, this fit of $\overline{Y}/\overline{Y}_{cl} = \exp(-49\eta^2)$ is slightly wider than the data, while in others, it is slightly narrower than the data, but overall does a fairly good job of predicting the radial mass fraction profile. The thin black line is the expected distribution from literature of $\overline{Y}/\overline{Y}_{cl} = \exp(-59\eta^2)$ (for room temperature jets) [37, 38, 52]. In most cases, this literature fit is narrower than our fit.

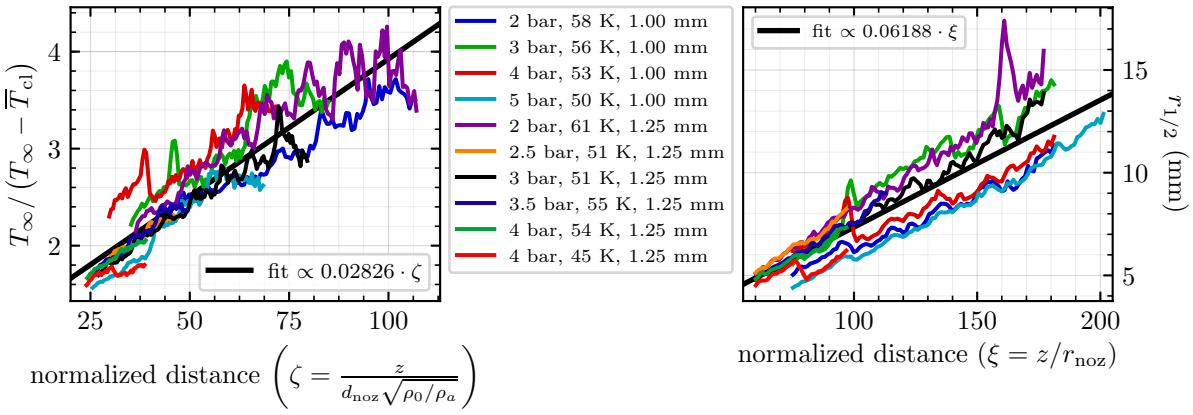

Figure 4-6 Normalized inverse centerline temperature decay (right) and temperature half-width (right) plotted as a function of the normalized downstream distance.

4.4. Centerline temperature decay rate and half width decay rate

The Raman scattering technique used in this study also allowed the measurement of temperature. Similar to Fig. 4-4, the normalized inverse average centerline temperature and half-width are plotted as a function of the normalized distance in Fig. 4-6. In this case, we are not aware of any literature data to which these decay rates can be compared. Also comparing the inverse centerline average temperature decay rate to the inverse average mass fraction decay rate makes little sense, because the normalization of the temperature is so much different from the inverse mass fraction. But the half-width decay rates can be compared. In this case, the temperature half-width decays at a slightly lower rate of 0.062, than the mass fraction half-width decay rate of 0.065. One-dimensional modeling of jets [27, 28] typically involves specifying the ratio of the half-width for different parameters (velocity, mole fraction, etc.) and this data will be used to better fit these models for cryogenic hydrogen jets.

The normalized temperature profiles are shown in Fig. 4-7. Similar to Fig. 4-5, the red line is the Gaussian fit for the release conditions of each frame, and the thick dashed black line is the second Gaussian fit for all the different release conditions. The thin black line is the literature fit to the normalized mass fraction profile (since there was no equivalent literature data for temperature). The normalized temperature profiles are slightly wider than the mass fraction profiles. The coefficient in the Gaussian fits for normalized temperature range from 21-49, with a fit to all of the data of $\Theta = \exp(-42\eta^2)$. The atmospheric temperature, T_∞ was a parameter for the Gaussian fit, and the best-fit value ranges from 292-300 K. This is near the average lab temperature of 295 K, with the scatter due to challenges with data analysis and the amount of noise on the temperature profiles (see Fig. 4-1).

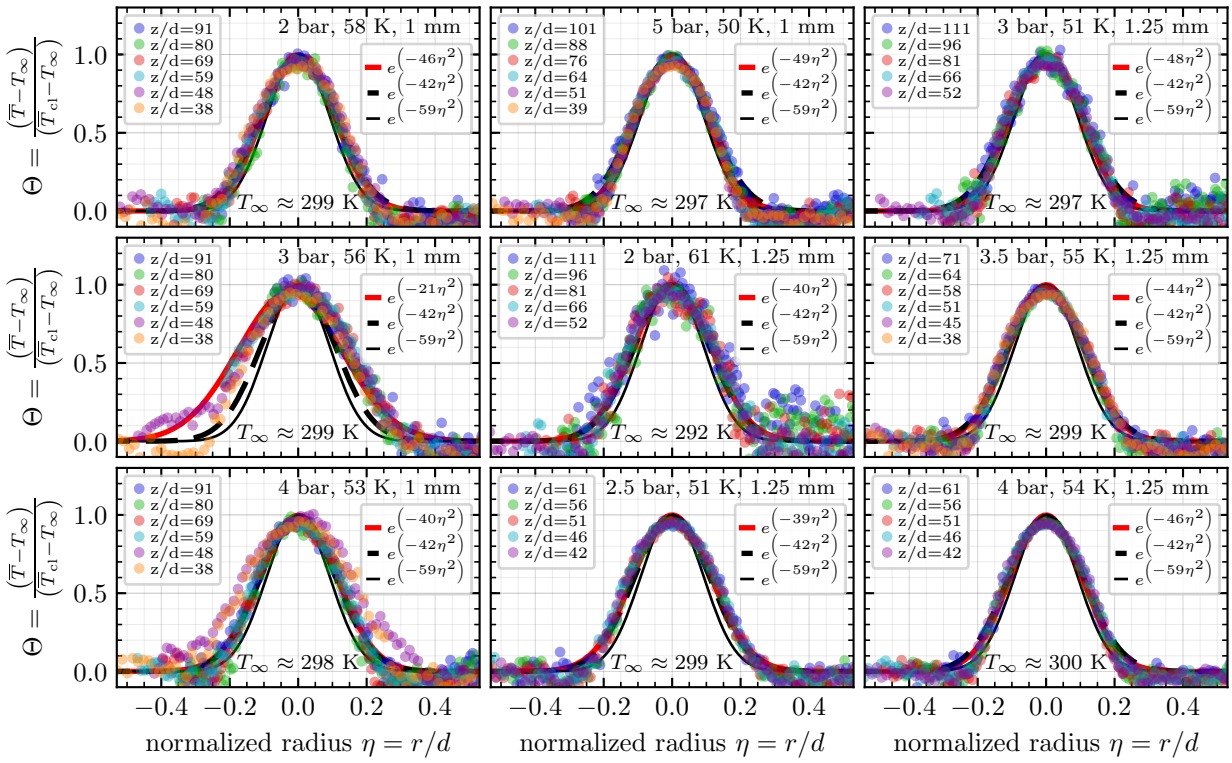

Figure 4-7 Radial temperatures at selected distances, normalized by the temperature excursion from the atmosphere. Three fits are shown on the graph. The red line is the fit for each condition (at all heights, not just the selected), the dashed thick black line is the fit for all 9 release conditions, and the thin black line is the literature fit for mass fraction [37, 38, 52].

4.5. Comparison to COLDPLUME model

Finally, the data was compared to the COLDPLUME model developed by Winters and Houf [27, 28]. As shown in Fig. 4-8, in some of these frames, the measured mole fraction and temperature fields at certain imaging heights were laterally offset significantly from the other imaging planes, likely due to ice at the nozzle. It should be noted that shifts out of the imaging plane are also likely in this setup, which will add error to the measurements. To correct for the lateral offset (no correction is possible for the out of plane offset), the maximum median mole fraction was determined, and the hydrogen, nitrogen, and temperature images were each shifted for each slice in the z-direction. Large shifts to the right of the images at some heights are especially evident for the 3 bar, 56 K, 1 mm release, where the experimental contours are jagged on the left hand side of the images. In most cases, the experimental contours for mole fraction are penetrating slightly further downstream than those predicted by the model. The widths of the mole fraction profiles are fairly well predicted by the model, and overall, the model is similar to the data. Cold temperatures (Fig. 4-8b) do not seem to penetrate as far as predicted by the model, while the experimental temperature widths are similar to the model predictions. It is obvious in these contour plots that there is significant noise in the temperature data, and this additional noise should be taken into account during model validation.

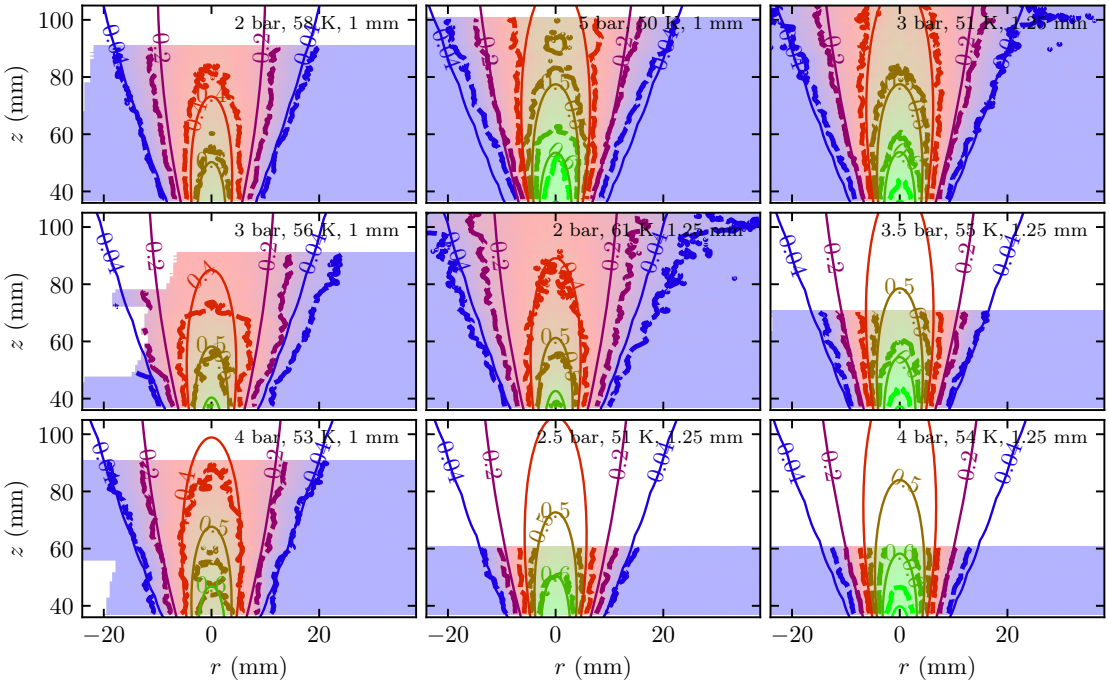

(a) Mole fraction fields. Contours are at mole fractions of 0.04 (the lean flammability limit for hydrogen), 0.2, 0.4, 0.5, and 0.6.

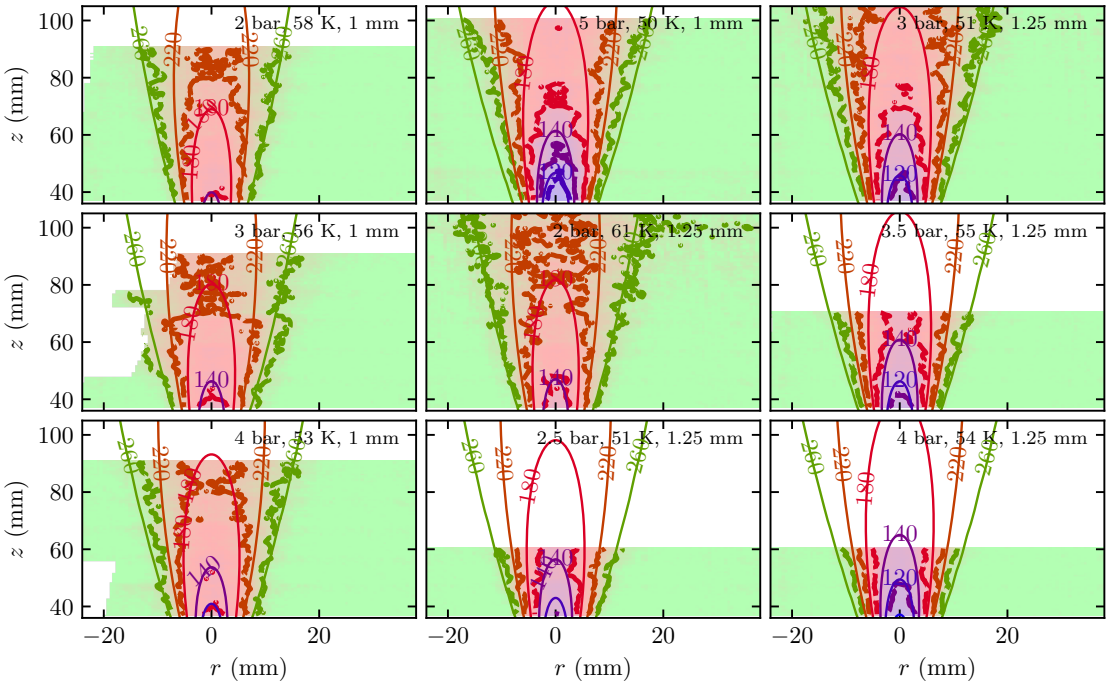

(b) Temperature fields. Contours are at 100, 120, 140, 180, 220, and 260 K.

Figure 4-8 Comparison of the model predictions shown by the solid, thin lines, to the experimental data, shown by the thick, dashed lines and shading for (a) mole fraction (top) and (b) temperature (bottom).

5. CONCLUSIONS AND FUTURE WORK

Understanding the safety distances for ignition sources, and the radiative heat flux from a turbulent-jet flame release or flame issuing from a hydrogen storage system leak are issues of importance for the safe use of hydrogen. While there is extensive literature on high-pressure hydrogen jet-flames, there is a scarcity of data on cryogenic systems. In this work, cryogenic under-expanded hydrogen jet flames were investigated over a range of temperature (37–295 K), pressure (2–6 bar_{abs}) and nozzle release diameters (0.75–1.25 mm). Measurements included the maximum ignition distance, the flame length, and the radiative heat flux.

This maximum ignition distance is greater for colder, cryogenic jets at a fixed hydrogen mass flow rate, than for room temperature jets. However, there is a linear dependence of the maximum ignition distance with the jet effective diameter. The mean hydrogen mass fraction along the centerline and the air entrainment rate both scale linearly with the effective diameter. The ignitability of a fuel-air mixture depends on the local mass fraction of the fuel, justifying the correlation between ignition distance and effective diameter. A model was applied to these releases and the mean mole fraction at ignition is approximately 0.14 (with 90% of the data between 0.13 and 0.18), with negligible dependence on temperature.

The hydrogen jet flame length (normalized by the release diameter) is linearly dependent on the square root of jet Reynolds number, for cryogenic, as well as room temperature sources of hydrogen. This observation is similar to the findings by Molkov and Saffers [42]. The maximum radiative heat flux is emitted at approximately 70–80% of the flame length. For a fixed hydrogen mass flow, the radiative heat flux increases as the release temperature decreases. This is due to the lower choked flow velocity of the colder hydrogen source increasing the flame residence time.

Raman imaging was used to characterize unignited cryogenic hydrogen jets. The average centerline mass fraction was observed to decay at a similar rate to room temperature releases of hydrogen, or other gases. The average half-width of the mass fraction jet, on the other hand, decayed more slowly than literature values of warmer jets. In order for mass to be conserved in models of these flows, empirical parameters such as the relative velocity and concentration profile spreading rates, and the entrainment rate will likely need to be modified from the values for warmer hydrogen. Radial profiles of the normalized hydrogen mass fraction and temperature show that these distributions are Gaussian and self-similar as a function of the radius normalized by the downstream distance. The normalized temperature is slightly wider than the normalized mass-fraction. Decay rates for the temperature magnitude and half-width were also measured in this work. Finally, the measured profiles were compared to a COLDPLUME model. Both the measured temperature and mass fraction fields agreed with those predicted by the model, although improvements may be possible with empirical parameter adjustment. This study provides critical information with regard to the development of guidelines for safety codes and standards of hydrogen infrastructure.

We plan to use this data to modify the COLDPLUME model and ensure accuracy for cryogenic hydrogen jets. We plan to evaluate the errors and error propagation in our data analysis before making any modifications to the model. We also plan on taking data at lower temperatures, although air-icing around the nozzle does become troublesome, changing the trajectory of the

release, at temperatures below 50 K. Icing at the nozzle can shift the release laterally, making stitching the images at different heights challenging and can shift the trajectory out of plane, such that we may not be measuring the jet across the centerline, causing challenges in data interpretation. Finally, we plan on attempting to measure velocity fields of these cryogenic jets using particle imaging velocimetry, potentially using the entrained moisture as the particle imaging medium.

The small diameters of the releases in this work are likely of similar size to those that might be expected from a leaking seal from a part in liquid hydrogen service. There are other scenarios that might be of concern to the hydrogen safety community, such as a full liquid hydrogen line shear where pooling and vaporization occur, or a lower velocity flow from a larger opening as would be encountered at a vent stack. Our group is planning to scale-up the Raman imaging diagnostic and apply it to larger releases to ensure that the model can also accurately predict these other scenarios.

REFERENCES

[1] California Fuel Cell Partnership. *Stations Map*. Available at https://cafcp.org/stationmap.

[2] California Fuel Cell Partnership. *The California Fuel Cell Revolution: A Vision for Advancing Economic, Social, and Environmental Priorities*. Tech. rep. Available online at https://cafcp.org/sites/default/files/CAFCR.pdf. 2018.

[3] *2019 Annual Evaluation of Hydrogen Fuel Cell Electric Vehicle Deployment and Hydrogen Fuel Station Network Development*. Tech. rep. Available at https://ww2.arb.ca.gov/sites/default/files/2019-07/AB8_report_2019_Final.pdf. California Environmental Protection Agency Air Resources Board, July 2019.

[4] *Nikola Corp*. Online at https://nikolamotor.com/.

[5] *NFPA 2: Hydrogen Technologies Code*. Tech. rep. National Fire Protection Association, 2016.

[6] J. LaChance. "Risk-informed separation distances for hydrogen refueling stations". *Int. J. Hydrogen Energy* 34 (2009), 5838–5845.

[7] J LaChance, W. Houf, B. Middleton, and L. Fluer. *Analyses to support development of risk-informed separation distances for hydrogen codes and standards*. Tech. rep. SAND2009-0874. Sandia National Laboratories, 2009.

[8] I. W. Ekoto, E. S. Hecht, C. San Marchi, K. M. Groth, C. LaFleur, N. Natesan, M. C. M, and A. Harris. *Liquid Hydrogen Release and Behavior Modeling: State-of-the-Art Knowledge Gaps and Research Needs for Refueling Infrastructure Safety*. Tech. rep. SAND2014-18776. Sandia National Laboratories, 2014.

[9] P. Hooker, D. B. Willoughby, and M. Royle. "Experimental releases of liquid hydrogen". In: *Proc. 4th Int. Conf. on Hydrogen Safety*. San Francisco, CA, Sept. 2011.

[10] M. Royle and D. Willoughby. *Releases of unignited liquid hydrogen*. Tech. rep. RR986. Health and Safety laboratory, 2014.

[11] A. Kotchourko, D. Baraldi, P. Bénard, N. Eisenreich, T. Jordan, J. Keller, A. Kessler, J. LaChance, V. Molkov, M. Steen, et al. "State of the art and research priorities in hydrogen safety". *Joint Research Centre of the European Commission (JRC)* (2014).

[12] J. E. Hall, P. Hooker, and D. Willoughby. "Ignited releases of liquid hydrogen: Safety considerations of thermal and overpressure effects". *Int. J. Hydrogen Energy* 39 (2014), 20547–20553.

[13] D. K. Pritchard and W. M. Rattigan. "Hazards of liquid hydrogen RR769 Position paper" (2010).

[14] D. Schmidt, U. Krause, and U. Schmidtchen. "Numerical simulation of hydrogen gas releases between buildings". *Int. J. Hydrogen Energy* 24 (1999), 479–488.

[15] J. Statharas, A. Venetsanos, J. Bartzis, J. Würtz, and U. Schmidtchen. "Analysis of data from spilling experiments performed with liquid hydrogen". *J. Hazard. Mater.* 77 (2000), 57–75.

[16] P. Middha and O. Hansen. “CFD simulation study to investigate the risk from hydrogen vehicles in tunnels”. *Int. J. Hydrogen Energy* 34 (2009), 5875–5886.

[17] P. Middha, M. Ichard, and B. Arntzen. “Validation of CFD modelling of LH2 spread and evaporation against large-scale spill experiments”. *Int. J. Hydrogen Energy* 36 (2011), 2620–2627.

[18] M. Ichard, O. Hansen, P. Middha, and D. Willoughby. “CFD computations of liquid hydrogen releases”. *Int. J. Hydrogen Energy* 37 (2012), 17380–17389.

[19] S. Giannissi, A. Venetsanos, N. Markatos, and J. Bartzis. “CFD modeling of hydrogen dispersion under cryogenic release conditions”. *Int. J. Hydrogen Energy* 39 (2014), 15851–15863.

[20] A. Venetsanos and S. Giannissi. “Release and dispersion modeling of cryogenic under-expanded hydrogen jets”. *Int. J. Hydrogen Energy* 42 (2017), 7672–7682.

[21] S. Giannissi and A. Venetsanos. “Study of key parameters in modeling liquid hydrogen release and dispersion in open environment”. *Int. J. Hydrogen Energy* 43 (2018), 455–467.

[22] T. Jin, M. Wu, Y. Liu, G. Lei, H. Chen, and Y. Lan. “CFD modeling and analysis of the influence factors of liquid hydrogen spills in open environment”. *Int. J. Hydrogen Energy* 42 (2017), 732–739.

[23] Y. Liu, J. Wei, G. Lei, Y. Lan, H. Chen, and T. Jin. “Dilution of hazardous vapor cloud in liquid hydrogen spill process under different source conditions”. *Int. J. Hydrogen Energy* 43 (2018), 7643–7651.

[24] R. Witcofski and J. Chirivella. “Experimental and analytical analyses of the mechanisms governing the dispersion of flammable clouds formed by liquid hydrogen spills”. *Int. J. Hydrogen Energy* 9 (1984), 425–435.

[25] U. Schmidtchen, L. Marinescu-Pasoi, K. Verfondern, V. Nickel, B. Sturm, and B. Dienhart. “Simulation of accidental spills of cryogenic hydrogen in a residential area”. *Cryogenics* 34 (1994), 401 –404.

[26] J. Xiao, J. Travis, and W. Breitung. “Hydrogen release from a high pressure gaseous hydrogen reservoir in case of a small leak”. *Int. J. Hydrogen Energy* 36 (2011), 2545–2554.

[27] W. S. Winters and W. G. Houf. “Simulation of small-scale releases from liquid hydrogen storage systems”. *Int. J. Hydrogen Energy* 36 (2011), 3913–3921.

[28] W. Houf and W. Winters. “Simulation of high-pressure liquid hydrogen releases”. *Int. J. Hydrogen Energy* 38 (2013), 8092–8099.

[29] A. Friedrich, W. Breitung, G. Stern, A. Veser, M. Kuznetsov, G. Fast, B. Oechsler, N. Kotchourko, T. Jordan, J. Travis, J. Xiao, M. Schwall, and M. Rottenecker. “Ignition and heat radiation of cryogenic hydrogen jets”. *Int. J. Hydrogen Energy* 37 (2012), 17589–17598.

[30] T. X. Phuoc, C. White, and D. McNeill. “Laser spark ignition of a jet diffusion flame”. *Optics and Lasers in Engineering* 38 (2002), 217 –232.

[31] T. C. Williams and C. R. Shaddix. “Simultaneous correction of flat field and nonlinearity response of intensified charge-coupled devices”. *Rev. Sci. Instrum.* 78 (2007).

[32] J. W. Leachman, R. T Jacobsen, S. G. Penoncello, and E. W. Lemmon. “Fundamental Equations of State for Parahydrogen, Normal Hydrogen, and Orthohydrogen”. *J. Phys. Chem. Ref. Data* 38 (2009), 721.

[33] F. P. Ricou and D. Spalding. “Measurements of entrainment by axisymmetrical turbulent jets”. *Journal of fluid mechanics* 11 (1961), 21–32.

[34] D. Han and M. Mungal. “Direct measurement of entrainment in reacting/nonreacting turbulent jets”. *Combustion and flame* 124 (2001), 370–386.

[35] X. Li, E. S. Hecht, and D. M. Christopher. “Validation of a reduced-order jet model for subsonic and underexpanded hydrogen jets”. *International Journal of Hydrogen Energy* 41 (2016), 1348–1358.

[36] R. Schefer, G. Evans, J Zhang, A. Ruggles, and R Greif. “Ignitability limits for combustion of unintended hydrogen releases: Experimental and theoretical results”. *international journal of hydrogen energy* 36 (2011), 2426–2435.

[37] A. J. Ruggles. “Statistically advanced, self-similar, radial probability density functions of atmospheric and under-expanded hydrogen jets”. *Exp. Fluids* 56 (2015), 202.

[38] A. J. Ruggles and I. W. Ekoto. “Ignitability and mixing of underexpanded hydrogen jets”. *Int. J. Hydrogen Energy* 37 (2012), 17549–17560.

[39] A Veser, M Kuznetsov, G Fast, A Friedrich, N Kotchourko, G Stern, M Schwall, and W Breitung. “The structure and flame propagation regimes in turbulent hydrogen jets”. *international journal of hydrogen energy* 36 (2011), 2351–2359.

[40] G Kalaghatigi. “Lift-off heights and visible lengths of vertical turbulent jet diffusion flames in still air”. *Combustion Science and Technology* 41 (1984), 17.

[41] R. Schefer, W. Houf, B Bourne, and J Colton. “Spatial and radiative properties of an open-flame hydrogen plume”. *International journal of hydrogen energy* 31 (2006), 1332–1340.

[42] V. Molkov and J.-B. Saffers. “Hydrogen jet flames”. *International journal of hydrogen energy* 38 (2013), 8141–8158.

[43] R. Schefer, W. Houf, T. Williams, B Bourne, and J Colton. “Characterization of high-pressure, underexpanded hydrogen-jet flames”. *International Journal of Hydrogen Energy* 32 (2007), 2081–2093.

[44] T Mogi, H Nishida, and S Horiguchi. “Flame Characteristics of high-pressure hydrogen gas jet”. In: *First International Conference on Hydrogen Safety, Pisa, Italy, Sept*. 2005, pp. 8–10.

[45] T. Imamura, S. Hamada, T. Mogi, Y. Wada, S. Horiguchi, A. Miyake, and T. Ogawa. “Experimental investigation on the thermal properties of hydrogen jet flame and hot currents in the downstream region”. *Int. J. Hydrogen Energy* 33 (2008), 3426–3435.

[46] E. Studer, D. Jamois, S. Jallais, G. Leroy, J. Hebrard, and V. Blancheti??re. “Properties of large-scale methane/hydrogen jet fires”. *Int. J. Hydrogen Energy* 34 (2009), 9611–9619.

[47] C. Proust, D. Jamois, and E. Studer. “High pressure hydrogen fires”. *Int. J. Hydrogen Energy* 36 (2011), 2367–2373.

[48] W Houf and R Schefer. “Predicting radiative heat fluxes and flammability envelopes from unintended releases of hydrogen”. *Int. J. Hydrogen Energy* 32 (2007), 136–151.

[49] I. H. Bell, J. Wronski, S. Quoilin, and V. Lemort. “Pure and pseudo-pure fluid thermophysical property evaluation and the open-source thermophysical property library coolprop”. *Ind. Eng. Chem. Res.* 53 (2014), 2498–2508.

[50] S. R. Turns and F. H. Myhr. “Oxides of nitrogen emissions from turbulent jet flames: Part I-Fuel effects and flame radiation”. *Combust. Flame* 87 (1991), 319–335.

[51] A. Molina, R. W. Schefer, and W. G. Houf. “Radiative fraction and optical thickness in large-scale hydrogen-jet fires”. *Proc. Combust. Inst.* 31 (2007), 2565–2572.

[52] C. D. Richards and W. M. Pitts. “Global density effects on the self-preservation behaviour of turbulent free jets”. *J. Fluid Mech.* 254 (1993), 417.

[53] R. Schefer, W. Houf, and T. Williams. “Investigation of small-scale unintended releases of hydrogen: momentum-dominated regime”. *Int. J. Hydrogen Energy* 33 (2008), 6373–6384.

DISTRIBUTION

Email—External

Name	Company Email Address	Company Name
Jennifer Hamilton	jhamilton@cafcp.org	California Fuel Cell Partnership
Pratikash Panda	pratikashp@iisc.ac.in	Indian Institute of Science

Email—Internal

Name	Org.	Sandia Email Address
Ethan Hecht	8367	ehecht@sandia.gov
Bikram Roy Chowdhury	8367	broycho@sandia.gov
Jon Zimmerman	8367	jzimmer@sandia.gov
Dongmei Mei	8635	dye@sandia.gov
Chris LaFleur	8854	aclafle@sandia.gov
CA Technical Library	8551	cateclib@sandia.gov

Sandia National Laboratories

Sandia National Laboratories is a multimission laboratory managed and operated by National Technology & Engineering Solutions of Sandia LLC, a wholly owned subsidiary of Honeywell International Inc., for the U.S. Department of Energy's National Nuclear Security Administration under contract DE-NA0003525.